Astronomy
&
Astrophysics

Fueling the central engine of radio galaxies

II. The footprints of AGN feedback on the ISM of 3C 236[*,**]

A. Labiano[1], S. García-Burillo[2], F. Combes[3], A. Usero[2], R. Soria-Ruiz[2],
G. Tremblay[4], R. Neri[5], A. Fuente[2], R. Morganti[6,7], and T. Oosterloo[6,7]

[1] Centro de Astrobiología, CSIC-INTA, Carretera de Ajalvir km. 4, 28850 Torrejón de Ardoz, Madrid, Spain
e-mail: alvaro.labiano@cab.inta-csic.es
[2] Observatorio Astronómico Nacional, Alfonso XII, 3, 28014 Madrid, Spain
[3] Observatoire de Paris, LERMA, CNRS, UMR 8112, 61 Av. de l'Observatoire, 75014 Paris, France
[4] European Southern Observatory, Karl-Schwarzschild-Str. 2, 85748 Garching bei München, Germany
[5] IRAM, 300 rue de la Piscine, Domaine Universitaire, 38406 Saint-Martin d'Hères Cedex, France
[6] Netherlands Foundation for Research in Astronomy, Postbus 2, 7990 AA Dwingeloo, The Netherlands
[7] Kapteyn Astronomical Institute, University of Groningen, PO Box 800, 9700 AV Groningen, The Netherlands

ABSTRACT

Context. There is growing observational evidence of active galactic nuclei (AGN) feedback on the interstellar medium (ISM) of radio-quiet and radio-loud galaxies. While AGN feedback is expected to be more common at high-redshift objects, studying local universe galaxies helps to better characterize the different manifestations of AGN feedback.
Aims. Molecular line observations can be used to quantify the mass and energy budget of the gas affected by AGN feedback. We study the emission of molecular gas in 3C 236, a Faranoff-Riley type 2 (FR II) radio source at $z \sim 0.1$, and search for the footprints of AGN feedback. The source 3C 236 shows signs of a reactivation of its AGN triggered by a recent minor merger episode. Observations have also previously identified an extreme H I outflow in this source.
Methods. The IRAM Plateau de Bure interferometer (PdBI) was used to study the distribution and kinematics of molecular gas in 3C 236 by imaging with high spatial resolution (0.6″) the emission of the 2–1 line of ^{12}CO in the nucleus of the galaxy. We searched for outflow signatures in the CO map. We also derived the star-formation rate (SFR) in 3C 236 using data available from the literature at UV, optical, and IR wavelengths, to determine the star-formation efficiency (SFE) of molecular gas.
Results. The CO emission in 3C 236 comes from a spatially resolved ∼1.4″(2.6 kpc-) diameter disk characterized by a regular rotating pattern. Within the limits imposed by the sensitivity and velocity coverage of the CO data, we do not detect any outflow signatures in the cold molecular gas. The disk has a cold gas mass $M(H_2) \sim 2.1 \times 10^9\ M_\odot$. Based on CO we determine a new value for the redshift of the source $z_{CO} = 0.09927 \pm 0.0002$. The similarity between the CO and H I profiles indicates that the deep H I absorption in 3C 236 can be accounted for by a rotating H I structure. This restricts the evidence of H I outflow to only the most extreme velocities. In the light of the new redshift value, the analysis of the ionized gas kinematics reveals a fast (∼1000 km s^{-1}) outflow. Outflow signatures in the CO emitting gas, are nevertheless absent in the warm molecular gas emission traced by infrared H$_2$ lines. The SFE in 3C 236 is consistent with the value measured in normal galaxies, which follow the canonical Kennicutt-Schmidt (KS) relation. This result, confirmed to hold in other young radio sources examined in this work, is in stark contrast with the SFE that is lower by a factor 10–50 that has been claimed to characterize evolved powerful radio galaxies.
Conclusions. There are no signs of ongoing AGN feedback to the molecular ISM of 3C 236. The recent reactivation of the AGN in 3C 236 (about 10^5 yr ago) is a likely explanation for the early evolutionary status of its molecular disk.

Key words. galaxies: individual: 3C 236 – galaxies: ISM – galaxies: kinematics and dynamics – ISM: jets and outflows – galaxies: active

1. Introduction

Active galactic nuclei (AGN) release vast amounts of energy into the interstellar medium (ISM) of their host galaxies. This energy input can heat gas in the ISM, preventing its collapse and inhibiting star formation. It may also expel the gas of the ISM in the form of winds (outflows), which deplete the host of star-forming fuel. This transfer of energy from the AGN to the host is known as AGN feedback. This could be responsible for the correlations between black hole and host galaxy bulge mass (Magorrian et al. 1998; Tremaine et al. 2002; Marconi & Hunt 2003; Häring & Rix 2004). It can also explain the fast transition of early-type galaxies from the blue cloud to the red sequence (Schawinski et al. 2007; Kaviraj et al. 2011).

Over the past decade, AGN feedback has been increasingly included in models of galaxy evolution (King 2003; Granato et al. 2004; Di Matteo et al. 2005; Croton et al. 2006; Ciotti & Ostriker 2007; Menci et al. 2008; King et al. 2008; Merloni & Heinz 2008; Narayanan et al. 2008; Silk & Nusser 2010).

Observational searches for signatures of AGN feedback have also grown in number (Thomas et al. 2005; Murray et al. 2005; Schawinski et al. 2006; Müller Sánchez et al. 2006; Feruglio et al. 2010; Crenshaw et al. 2010; Fischer et al. 2011; Villar-Martín et al. 2011; Dasyra & Combes 2011; Sturm et al. 2011; Maiolino et al. 2012; Aalto et al. 2012). Yet, observational evidence of AGN feedback is still fragmentary.

The AGN feedback takes place through two mechanisms: the *radiative* or *quasar* mode, and the *kinetic* or *radio* mode. In the quasar mode, the radiation from the AGN dominates the energy transfer to the ISM. In the radio mode, the momentum of the jet is transferred to the ISM.

The most dramatic effects of the kinetic mode are seen in powerful radio galaxies. With jets up to several Mpc-size, they can inject enormous amounts of energy, not only into their host galaxy ISM, but also into the intergalactic medium (IGM) of the galactic group or cluster where they reside (e.g., Bîrzan et al. 2004; Fabian et al. 2006; McNamara & Nulsen 2007, 2012). It is thought that a significant fraction of massive galaxies undergo a radio galaxy phase at least once in their lifetime (e.g., Best et al. 2006). Consequently, understanding how AGN feedback works during this phase is crucial for a better understanding of galaxy evolution.

Observations of H I and ionized gas in radio galaxies have found massive outflows in a significant number of radio galaxies at different redshift ranges (e.g., Morganti et al. 2003a; Rupke et al. 2005; Holt et al. 2006; Nesvadba et al. 2006, 2008; Lehnert et al. 2011). Even though molecular gas may dominate the mass/energy budget of the wind, unambiguous evidence of a molecular outflow has thus far only been found in one radio galaxy (4C 12.50; Dasyra & Combes 2011). Another manifestation of AGN feedback, the inhibition of star formation, has also been claimed to be at work in radio galaxies. Nesvadba et al. (2010) used the 7.7 μm polycyclic aromatic hydrocarbons (PAH) emission to estimate the star-formation rate (SFR) in a sample of radio galaxies. Based on their estimated molecular gas contents, Nesvadba et al. (2010) found that radio galaxies in their sample are ~10–50 times less efficient in forming stars compared to normal galaxies that follow the canonical Kennicutt-Schmidt relationship (Schmidt 1959; Kennicutt 1998). The warm-H_2 emission of these radio galaxies suggests the presence of shocks in the warm molecular gas traced by a set of IR H_2 lines. These shocks, identified in the warm-H_2 phase, would increase the turbulence in the molecular ISM as a whole, inhibiting the star formation in the host. However, it is still an open question whether shocks are affecting the bulk of the molecular ISM or if they only concern the warm molecular gas phase. CO observations, which are well adapted to trace most of the molecular ISM, are the key to understanding the complexity of how AGN feedback affects the kinematics and the star-formation properties of molecular gas in radio galaxies.

The source 3C 236 is the second-largest radio galaxy in the Universe (~4.5 Mpc deprojected size, Willis et al. 1974; Barthel et al. 1985)[1]. Its radio structure shows an old (2.6×10^8 yr), classical double, FR II source (Fanaroff & Riley 1974) on large scale maps, and a younger (10^5 yr), ~2 kpc compact steep-spectrum source (CSS, O'Dea 1998) in the center, which is responsible for two thirds of the total radio emission of 3C 236 (Schilizzi et al. 2001). Both structures are roughly aligned and oriented at an angle ~30° to the plane of the sky, with the northwest jet

approaching (Schilizzi et al. 2001). The double-double morphology (CSS + large-scale source; e.g., Schoenmakers et al. 2000; Kaiser et al. 2000) of 3C 236 is consistent with a reignition of the AGN activity, probably caused by a minor merger (O'Dea et al. 2001).

The host of 3C 236 is a massive (~10^{12-13} $M_\odot$, Sandage 1972; Strom & Willis 1980) elliptical galaxy (Barthel et al. 1985; Mezcua et al. 2011) with a distorted optical morphology at kpc scales (Smith & Heckman 1989), consistent with a merger. High-resolution imaging and optical broadband-filter absorption maps (de Koff et al. 2000) show an inner dust disk (0.5 kpc from the nucleus), and a broad, dynamically young, ~8 kpc long dust lane (1.5 kpc from the nucleus), misaligned by ~25° with the inner disk (Martel et al. 1999; de Koff et al. 2000). The total mass of the whole dust system is ~10^7 $M_\odot$ (de Koff et al. 2000; Sodroski et al. 1994).

The total stellar mass of 3C 236 has been estimated to be 10^{12} $M_\odot$ (Tadhunter et al. 2011), consisting of a young ($\lesssim 10^7$ yr) and an old stellar population ($\gtrsim 10$ Gyr). The old stellar population represents 72% of the total stellar mass (see also Holt et al. 2007; Buttiglione et al. 2009). Using high-resolution optical and UV photometry, O'Dea et al. (2001), Baldi & Capetti (2008), and Tremblay et al. (2010) found young (~10^7 yr) star-forming knots on the edge of the dust lane, surrounding the nucleus, as well as and older (~10^9 yr) population in the nucleus. The star formation in the young knots could have been triggered by the infalling gas from the minor merger that reignited the AGN. However, it is not completely clear how the nuclear population relates to the AGN activity (Tremblay et al. 2010).

The star-formation history of 3C 236 and the possibly related reignition of its AGN make 3C 236 an ideal candidate for searches of AGN feedback signatures. Furthermore, 3C 236 is known to have a fast (~1500 km s^{-1}), massive (~50 $M_\odot$ yr^{-1}) H I outflow: Westerbork Radio Telescope spectra show a shallow, narrow blueshfited H I absorption component with a broad blue wing (Morganti et al. 2005). Previous searches of molecular gas in 3C 236 were plagued by limited sensitivity and they were undertaken with single-dish telescopes. Based on CO observations; made with the IRAM-30 m telescope in a sample of radio galaxies, Saripalli & Mack (2007) reported the non-detection of CO line emission in 3C 236; the implied upper limit on the molecular gas mass of 3C 236 (~2–3 $\times 10^9$ $M_\odot$) was not very compelling, however.

This is the second of a series of papers where we use interferometric observations of the molecular line emission to study the fueling and the feedback of activity in a sample of nearby radio galaxies (observations of 4C 31.04, a young compact symmetric object (CSO) source, were presented by García-Burillo et al. 2007). To this purpose, we have carried out 1 mm/3 mm continuum and ^{12}CO(2–1) line high-resolution and high-sensitivity observations of 3C 236 with the Plateau de Bure Interferometer (PdBI). We study the continuum emission of the source at 1 mm and 3 mm wavelengths and analyze the distribution and kinematics of molecular gas based on the emission of the ^{12}CO(2–1) line. We search for outflow signatures in the CO map and re-evaluate the evidence of outflow signatures in different ISM tracers. Furthermore, we derive the SFR of 3C 236 based on several tracers available from the literature. Based on the gas mass derived form CO emission and on the SFR estimates, we compare the star-formation efficiency of 3C 236 against a sample of powerful radio galaxies. Finally, we discuss a scenario consistent with the properties and the history of 3C 236 and its host.

---

[1] Machalski et al. (2008) recently reported the discovery of the currently largest radio galaxy, J1420–0545, with a projected size of 4.7 Mpc.
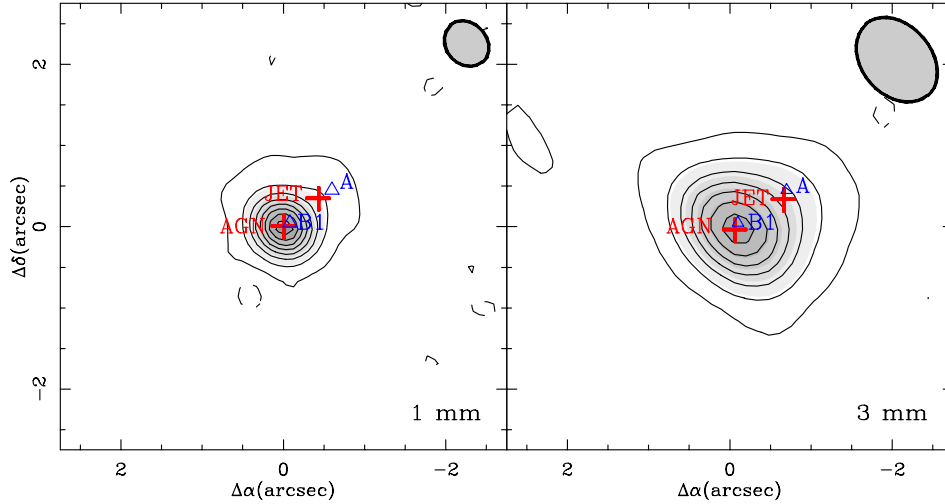
Fig. 1. Continuum maps of 3C 236 at 1 mm (*left*) and 3 mm (*right*). Crosses (+) mark the position of the AGN and jet peak emission according to the UV-FIT models (Table 1). Triangles mark the position of components A and B1 from the VLBI map of Schilizzi et al. (2001). The contour levels are -3 mJy beam^{-1}, 3 mJy beam^{-1}, 9 mJy beam^{-1} to 63 mJy beam^{-1} in steps of 9 mJy beam^{-1} for the 1 mm map, and -6 mJy beam^{-1}, 6 mJy beam^{-1}, 22 mJy beam^{-1} to 176 mJy beam^{-1} in steps of 22 mJy beam^{-1} for the 3 mm map. The filled ellipses represent the beams at 1 mm $(0.60'' \times 0.50''$, PA $= 41°)$ and 3 mm $(1.16'' \times 0.86''$, PA $= 41°)$. $(\Delta\alpha, \Delta\delta) = (0,0)$ corresponds to the position of the AGN at 1 mm in both panels.

2. Observations

2.1. Interferometer observations

The PdBI (Guilloteau et al. 1992) observations of 3C 236 were obtained in the ^{12}CO(2–1) 1mm line using six antennas in the array B configuration in January 2009. We assumed the optical redshift of the source derived by Holt (2005), $z = 0.10054$ (v_0(HEL) = 30 129 km s^{-1}) to tune the 1 mm receivers centered on the ^{12}CO(2–1) line redshifted to 209.504 GHz. The relative velocity scale, although re-determined in Sect. 4, initially refers to this redshift ($v-v_0$). With this setting we obtained a velocity coverage of ~1400 km s^{-1} at 209.5 GHz with the narrow band correlator of the PdBI (1 GHz-wide) and the two polarizations of the receiver. Observations were conducted in a single pointing of size ~23$''$. The adopted phase-tracking center of the observations was set at $(\alpha_{2000}, \delta_{2000}) = (10h06m01.7s, 34°54'10'')$, the position of the nucleus given by the NASA/IPAC Extragalactic Database (NED). Nevertheless, the position of the dynamical center determined in Sect. 3, which coincides with the position of the radio continuum VLBI core (Schilizzi et al. 2001), is $\simeq 1''$ offset to the NE with respect to the array center: $(\Delta\alpha, \Delta\delta) \sim (0.6'', 0.4'')$. Visibilities were obtained through on-source integration times of 22.5 min framed by short (2 min) phase and amplitude calibrations on the nearby quasars 0923+392 and 1040+244. The visibilities were calibrated using the antenna-based scheme. The absolute flux density scale was calibrated on MWC349 and found to be accurate to <10% at 209.5 GHz.

The image reconstruction was made with the standard IRAM/GILDAS software (Guilloteau & Lucas 2000)[2]. We used natural weighting and no taper to generate the CO line map with a size of 66$''$ and 0.13$''$ /pixel sampling, and obtained a synthesized beam of 0.60$''$ × 0.51$''$ @ PA = 41° at 1 mm. The 1σ point source sensitivity was derived from emission-free channels resulting in 1.1 mJy beam^{-1} in 20 MHz (~29 km s^{-1})-wide channels. We obtained a map of the continuum emission at 209.5 GHz averaging channels free of line emission from $v - v_0 = +100$ to $+640$ km s^{-1}. The corresponding 1σ sensitivity of the continuum emission is ~0.3 mJy beam^{-1} at 209.5 GHz.

We subsequently observed 3C 236 in the HCO$^+$(1–0) and HCN(1–0) transitions at 3 mm for six hours on January 2010. For these observations we tuned the receivers at a frequency intermediate between those of the HCO$^+$(1–0) (89.188 GHz) and HCN(1–0) (88.632 GHz) transitions redshifted to 81.017 GHz. The velocity coverage at 81 GHz was ~3700 km s^{-1}. We used the same phase-tracking center and redshift as adopted for the 1 mm observations described above. The twofold goal of the 3 mm observations was the detection of the HCO$^+$(1–0) and HCN(1–0) lines as well as of their underlying continuum emission. Notwithstanding, these lines were not detected down to the sensitivity limit (0.8 mJy beam^{-1} in 10 MHz, ~37 km s^{-1} -wide channels). A 3 mm continuum map was built inside the 59$''$ field-of-view using velocity channels away from any potential contribution of line emission in the signal sideband of the PdBI receivers ($v - v_0 = -1370$ to -1740 km s^{-1}). The corresponding 1σ sensitivity is ~0.3 mJy beam^{-1} at 81 GHz. We used natural weighting to generate the maps of the continuum emission and obtained a synthesized beam of 1.17$''$ × 0.86$''$ @ PA = 41°.

2.2. Ancillary data

We have used the following archival *Hubble* Space Telescope (HST) images: ACS/SBC/F140LP (hereafter FUV image), ACS/HRC/F555W (*V*-band), STIS/NUV-MAMA/F25SRF2 (NUV, O'Dea et al. 2001; Allen et al. 2002; Tremblay et al. 2010); WFPC2/F702W (*R*-band) and NICMOS2 (*H*-band) obtained by Sparks and collaborators (de Koff et al. 1996; McCarthy et al. 1997; Madrid et al. 2006; Tremblay et al. 2007; Floyd et al. 2008); H I data by Morganti et al. (2005); mid-IR data from Dasyra & Combes (2011) and Guillard et al. (2012); Sloan Digital Sky Survey (SDSS) spectra from York et al. (2000), Abazajian et al. (2009), and Buttiglione et al. (2009).

We use $H_0 = 71$, $\Omega_M = 0.27, \Omega_\Lambda = 0.73$ (Spergel et al. 2003) throughout the paper. Luminosity and angular distances are $D_L = 452$ Mpc and $D_A = 374$ Mpc; the latter gives a physical scale of 1$''$ = 1.8 kpc (Wright 2006).

3. Continuum maps

Figure 1 shows the continuum maps derived at 209.5 GHz and 81 GHz in the nucleus of 3C 236. The emission spreads on

---

[2] http://www.iram.fr/IRAMFR/GILDAS

Table 1. Point source models.

Component	Wavelength	RA (J2000)	Dec (J2000)	Flux (mJy)
AGN	1 mm	10 06 01.753	+34 54 10.425	71.4 ± 0.4
Jet	1 mm	10 06 01.717	+34 54 10.777	10.1 ± 0.4
AGN	3 mm	10 06 01.748	+34 54 10.385	150.4 ± 0.8
Jet	3 mm	10 06 01.699	+34 54 10.758	45.2 ± 0.8
VLBI core	6 cm	10 06 01.756	+34 54 10.460	–

Notes. AGN and jet positions in the 1 mm and 3 mm maps of 3C 236 according to the UV-FIT models. The VLBI position of the core (Schilizzi et al. 2001; Taylor et al. 2001) is included for comparison.

spatial scales significantly larger than the PdBI synthesized beam at both frequencies and consists of a dominant central component and a fainter emission component that extends to the NW of the source. We used the GILDAS task UV-FIT to fit the continuum visibilities at both frequencies with a set of two point sources. Table 1 lists the parameters of the best-fit solutions. Most of the flux comes from a central source located at $(\Delta\alpha, \Delta\delta) \sim (+0.6 \pm 0.1'', +0.4 \pm 0.1'')$ at both frequencies. This corresponds within the errors with the position of the AGN core determined in the VLBI 1.7 and 5 GHz maps (component B2 in Schilizzi et al. 2001; Taylor et al. 2001) and is therefore adopted as the best guess for the dynamical center of 3C 236 (component labeled "AGN" in Fig. 1). The NW 1 mm and 3 mm components are both fitted by a point source located at $(\Delta\alpha, \Delta\delta) \sim (+0.0 \pm 0.1'', +0.8 \pm 0.1'')$, i.e., at a position intermediate between the jet components A (radio lobe) and B1 (base of the radio jet) identified in the VLBI 1.7 and 5 GHz maps of Schilizzi et al. (2001) and Taylor et al. (2001). This indicates that the NW elongations identified in Fig. 1 are the mm-counterparts of the approaching radio jet of the inner region of 3C 236 (component labeled "jet" in Fig. 1). Using the fitted positions for the AGN and jet components, we derive a PA of 302° for the mm-jet(s); this is consistent with the orientation of the CSS radio jet determined in the VLBI cm-maps of the source.

To establish the nature of the 1 mm and 3 mm emissions of 3C 236 we have compared the fluxes of the fitted components ("AGN" and "jet") with the corresponding radio emissions between 10 MHz and 10 GHz of 3C 236 (available in NED). In the $\log f_\nu - \log \nu$ plot, the 1 mm and 3 mm data points are aligned with the radio data points, following a power law with spectral index $\simeq -0.9 \pm 0.1$. This spectral index is expected for synchrotron radiation from CSS sources (e.g., O'Dea 1998). Therefore, we conclude that the 1 mm and 3 mm emission in 3C 236 can be accounted for by synchrotron radiation.

4. CO maps

4.1. Distribution of molecular gas

We detect significant CO(2–1) emission above 3σ levels from $v - v_0 = -685$ to $+165$ km s^{-1}. Figure 2 shows the CO(2–1) intensity map obtained by integrating the emission within this velocity range with no threshold value adopted on the intensities. As illustrated in this figure, CO emission is detected at significant levels only in the inner diameter of 2'' (3.6 kpc) of 3C 236. The distribution of the molecular gas can be described as a spatially resolved elongated disk-like source. While the peak of CO emission lies close to the AGN, the detection of lower level emission that extends farther to the NE gives the overall impression that the molecular disk, which has a deconvolved major axis diameter of 1.3'' (2.3 kpc), is off-centered with respect to the AGN.
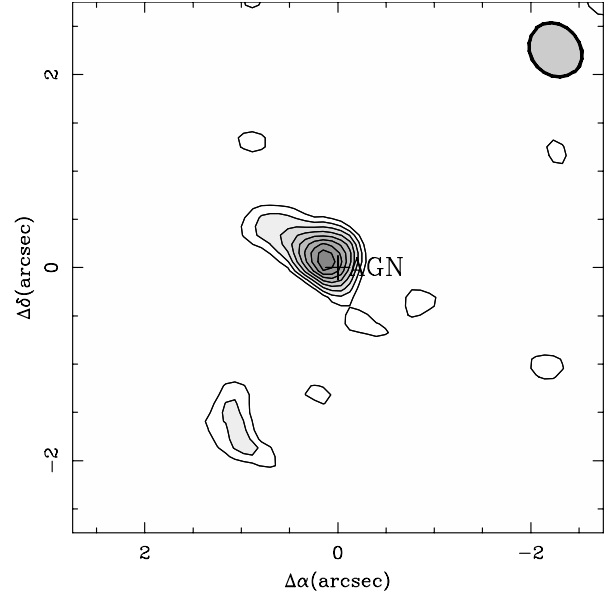

Fig. 2. ^{12}CO(2–1) intensity map of 3C 236, integrating all emission above 3σ levels, from $v - v_0 = -685$ to $+165$ km s^{-1}. The contour levels are 3σ, to 6.5σ in steps of 0.5σ, with $\sigma = 0.21$ Jy beam^{-1} km s^{-1}. $(\Delta\alpha, \Delta\delta)$-offsets in arcsec are relative to the location of the AGN. The gray ellipse shows the 1 mm beam.
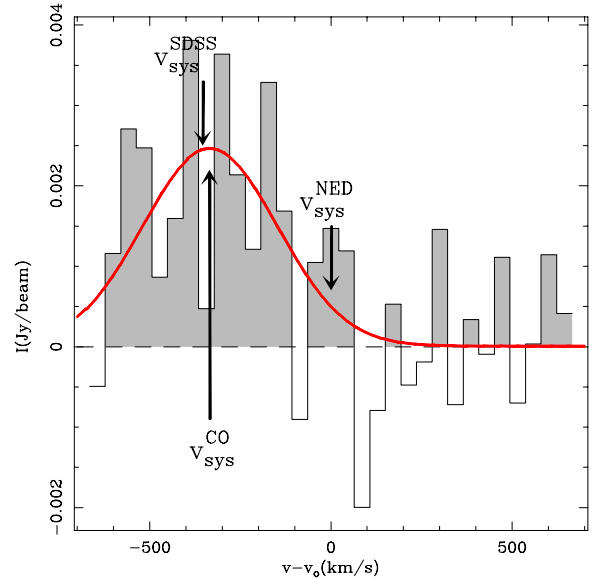

Fig. 3. Spectrum of the ^{12}CO(2–1) line emission (after subtracting the continuum emission) toward the AGN position of 3C 236 (histogram). The red solid line shows the Gaussian fit to the spectrum. Velocities in the x-axis are with respect to the redshift $z = 0.10054$ (v_0(HEL) = 30 129 km s^{-1}), where the PdBI narrow band correlator was centered. Arrows mark the heliocentric systemic velocity of 3C 236 according to SDSS (29 740 km s^{-1}), CO (29 761 km s^{-1}), and NED (30 129 km s^{-1}).

The observed asymmetry of the molecular disk can be partly attributed to the incomplete velocity coverage of the CO(2–1) emission in our data. As illustrated in Fig. 3, which shows the CO(2–1) spectrum observed toward the AGN, any potential emission at velocities $v - v_0 < -700$ km s^{-1} lies outside the range covered by the PdBI narrow band correlator, which was initially centered on our observations around $z = 0.10054$ (v_0(HEL) = 30 129 km s^{-1}). With this caveat in mind,

the Gaussian fit to the CO spectrum of Fig. 3 provides an upper limit to the systemic velocity (v_{sys}) of the source, assuming the plausible scenario where gas motions are driven by rotation at these radii. The shape of the CO line profile, which shows declining intensities at the low (blue) velocity end of the spectrum, nevertheless indicates that the true v_{sys} is close to the adopted value: $v - v_0 < -335$ km s^{-1}, which corresponds to v_{sys}^{CO}(HEL) $= 29\,761 \pm 40$ km s^{-1}. The implied upper limit on the redshift $z_{CO} = 0.09927 \pm 0.0002$ is significantly lower than the redshift adopted by Hill et al. (1996), who based their estimate on Paα and Hα measurements ($z = 0.10054$, Hill et al. 1996, and NED)[3]. The SDSS has a more recent optical spectrum of 3C 236 available. The redshift of the source based on the SDSS spectrum is $z = 0.0991 \pm 0.0001$ (v_{sys}(HEL) $= 29\,740 \pm 20$ km s^{-1}), which is also consistent within the errors with z_{CO}. In the light of the new redshift value derived from CO, we analyze in Sect. 5 the evidence of outflow signatures in different tracers of the ISM of 3C 236.

Figure 2 shows a CO emission component SE of the AGN, unrelated to the rest of the CO. The size of this component is larger than the beam, and the flux is higher than 3σ levels, an indication that this feature could be real. This component falls outside the outer dust disk and beyond the radio emission of the CSS source. It is also misaligned with the radio jets. There are no features in the VLBI, optical, and UV maps at the location of this component, so its origin is unknown.

Figure 4a shows the ^{12}CO(2$-$1) map superposed on the V–H color map made from HST imaging. The color map shows two prominent dust lane features that extend over significantly different spatial scales: the *outer* dust lane visualizes a highly inclined gas disk of $\sim$4.5$''$ (8.1 kpc)-major axis diameter oriented along $PA \simeq 55°$. The *inner* dust lane pictures a much smaller disk-like structure of $\sim$1$''$ (1.8 kpc)-major axis diameter oriented along $PA \simeq 30°$. The two concentric disks are thus misaligned, a characteristic already noted by O'Dea et al. (2001), who interpreted this as a signature of discrete accretion events. The inner disk is roughly perpendicular to the inner radio jet, oriented along $PA \simeq 302°$.

4.2. Kinematics of molecular gas

As shown in Fig. 4a, the CO disk seems to be closely linked to the *inner* dusty disk: to the limit of our sensitivity, CO emission is not detected in the *outer* disk. To better illustrate this association, we show in Fig. 4b the CO emission integrated in two channels defined to cover the ranges corresponding to *blue* velocities ($v_{sys}^{CO}$$-$330 km s^{-1} $< v < v_{sys}^{CO}$) and *red* velocities (v_{sys}^{CO} $< v < v_{sys}^{CO} + 485$ km s^{-1}). The velocity structure of the CO disk is spatially resolved in the maps: the emission peaks in the *red* and *blue* lobes are separated by $\simeq$0.45$''$, i.e., a significant fraction of the PdBI beam. Lower-level yet significant emission, which stands out more clearly in Fig. 4b than in Fig. 4a thanks to the narrower velocity channels used to generate the maps, extends up to radial distances $\sim$0.7$''$ (1.3 kpc) from the AGN. The line joining the peaks of the *blue* and *red* lobes has a PA = 28.07°, which is consistent with the orientation of the *inner* dusty disk.

Figure 5 shows the position–velocity (p$-$v) diagram taken along this line (PA = 28.07°), identified as the kinematical major axis of the CO disk. The kinematical pattern of

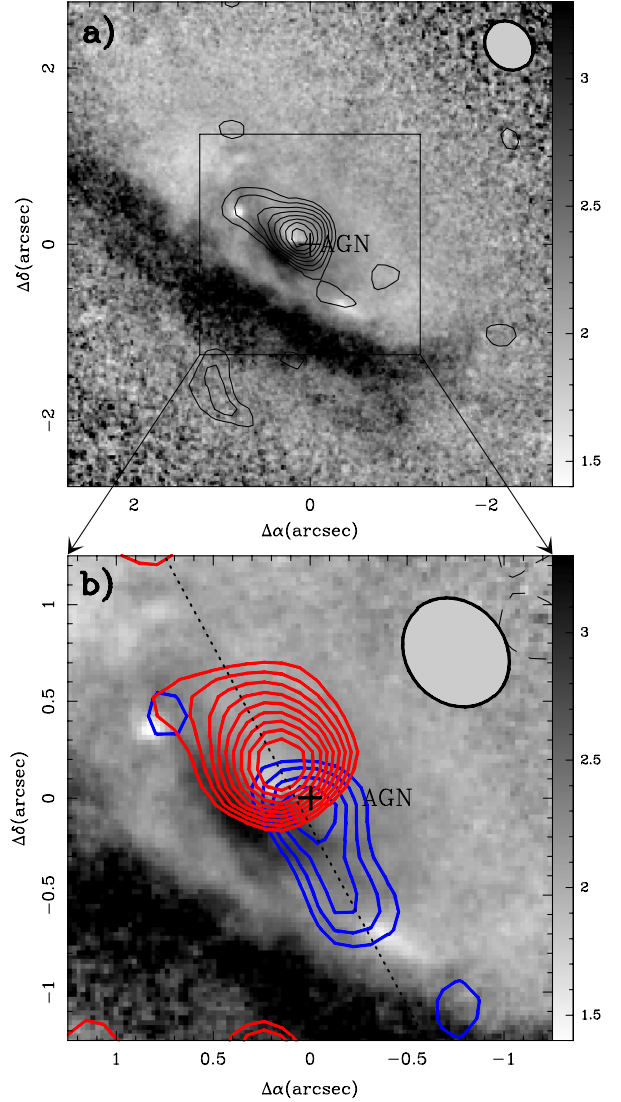[3] Hill et al. (1996) already noted that their redshift determination was significantly different from the previous estimate of Sandage (1967), who measured $z = 0.0989 \pm 0.0001$, i.e., in close agreement with the CO-based value.
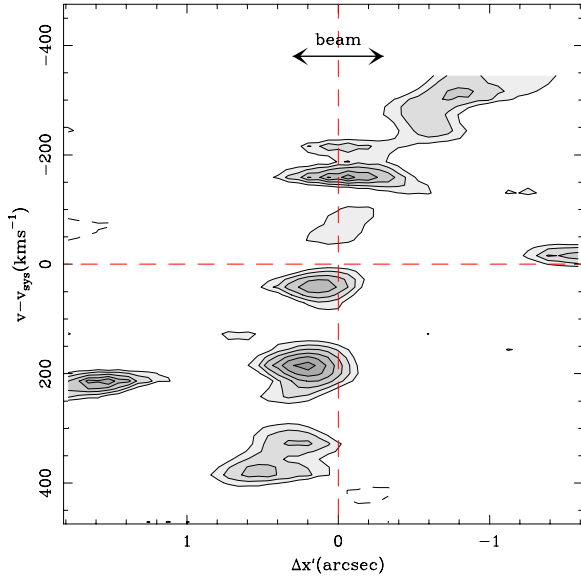
Fig. 4. **a)** V–H color map (gray scale in STmag magnitude system) of 3C 236, with the integrated ^{12}CO(2$-$1) emission overlaid. Contour levels as in Fig. 2. **b)** Zoom into the central 3$''$ of 3C 236. Contours represent the ^{12}CO(2$-$1) line maps of 3C 236 integrated in two channels: blue ($v_{sys}^{CO}$$-$330 km s^{-1} $< v < v_{sys}^{CO}$) and red (v_{sys}^{CO} $< v < v_{sys}^{CO} + 485$ km s^{-1}). The contour levels are 3σ to 4.5σ in steps of 0.5σ ($\sigma = 0.13$ Jy beam^{-1} km s^{-1}) for the blue channel, and 3σ to 7σ in steps of 0.5σ ($\sigma = 0.13$ Jy beam^{-1} km s^{-1}) for the red channel. The dashed line shows the major axis of the molecular gas disk. ($\Delta\alpha$, $\Delta\delta$)-offsets in arcsec are relative to the location of the AGN. The gray ellipses show the 1 mm beam. Color version available in electronic format.

the p$-$v diagram reveals the signature of a spatially resolved rotating molecular gas disk. At the NW edge of the CO disk, the radial velocity reaches $\sim$400 km s^{-1}. If we assume that the inclination of the gas disk is 60°, based on the orientation of the radio source (Schilizzi et al. 2001), we derive that $v_{rot} \sim 460$ km s^{-1} at $R \sim 1.2$ kpc. This is similar to the typical range of rotation velocities derived in other early-type galaxies (full width at zero intensity, $FWZI \lesssim 800$ km s^{-1}; e.g., Krips et al. 2010; Crocker et al. 2012, and references therein).

Based on a spherical mass distribution model, the dynamical mass M_{dyn} inside R, derived as $M_{dyn} = R \times v_{rot}^2 / G$ (where G is the gravitational constant, R is the de-projected radius of the disk, and v_{rot} is the de-projected radial velocity at the edge of the disk),

Fig. 5. Position–velocity diagram of the $^{12}CO(2-1)$ emission along the major axis of the molecular gas disk of 3C 236 (dashed line in Fig. 4). Positions (Δx) are relative to the AGN. Velocities are relative to the CO v_{sys}^{CO}. The contour levels are -2σ, 2σ to 4.5σ in steps of 0.5σ, with $\sigma = 3$ mJy beam^{-1} km s^{-1}.

is $\sim 6.1 \times 10^{10}$ $M_\odot$. Accounting for the mass of molecular gas derived in Sect. 4.3, we determine that the spheroidal stellar mass (M_{sph}) is $\sim 5.8 \times 10^{10}$ $M_\odot$ inside $R \sim 1.2$ kpc if the contribution from dark matter to M_{dyn} is neglected. Not surprisingly, this value falls short of accounting for the total stellar mass M_* of 3C 236, which amounts to 9.2×10^{11} $M_\odot$ according to the stellar population models of Tadhunter et al. (2011). This value, together with the available estimates of the supermassive black hole mass (M_{bh}) can be used to evaluate whether 3C 236 fits within the known $M_{bh}-M_{sph}$ relation followed by different galaxy populations. The two estimates for M_{bh} in 3C 236 published by Marchesini et al. (2004) ($M_{bh} = 4.2 \times 10^8$ $M_\odot$) and Mezcua et al. (2011) ($M_{bh} = 3.2 \times 10^8$ $M_\odot$) are in rough agreement. Taking the average of both estimates, the implied M_{bh}/M_{sph} ratio in 3C 236 is $\sim 0.05\%$. This is compatible within the errors with the M_{bh}/M_{sph} ratio predicted for radio-loud AGNs at $z \sim 0.1$, based on the redshift-dependent law found by McLure et al. (2006) (see Eq. (3) of their paper).

4.3. Mass of molecular gas

The total flux obtained within the 21″ primary beam field of the PdBI is 4 Jy km s^{-1}. Assuming a brightness temperature ratio CO(2–1)/CO(1–0)$\simeq$1, we can use the equations of Solomon et al. (1997) to derive the equivalent CO(1–0) luminosity: $L'_{CO} = 4.6 \times 10^8$ K km s^{-1} pc^{-2}. If we apply the Galactic ratio of H$_2$-mass to CO-luminosity (4.6 $M_\odot$/K km s^{-1} pc^2, Solomon et al. 1987), we estimate that the H$_2$ mass in 3C 236 is $M(H_2) = 2.1 \times 10^9$ $M_\odot$. Including the mass of helium, the corresponding total molecular gas mass is 2.9×10^9 $M_\odot$. The average column density of hydrogen atoms derived from CO is $N_{H,CO} = 9.4 \times 10^{22}$ cm^{-2}. The *Chandra* spectrum of 3C 236, which has a spatial resolution (~ 0.6″) similar to our observations, is best fitted by a power-law plus an absorption component with $N_{H,CO} = 2 \times 10^{22}$ cm^{-2} (Birkinshaw et al., in prep.). The column densities derived from CO and X-rays are thus consistent within a factor 4–5.

Strong emission from mid-IR H$_2$ rotational lines, a tracer of warm ($T_k > 100$ K) and diffuse ($n(H_2) \sim 10^3$ cm^{-3}) molecular hydrogen, has also been detected in 3C 236. The galaxy qualifies as a molecular hydrogen emission galaxy (MOHEG) due to its high H$_2$ to PAH(7.7 μm) luminosity ratio $L(H_2)/L(7.7\ \mu m) \geq 0.33$, i.e., well beyond the limit defined by Ogle et al. (2010): $L(H_2)/L(7.7\ \mu m) > 0.04$. Dasyra & Combes (2011) used *Spitzer* IRS to study the warm-H$_2$ emission lines ((0–0) S0 28.22 μm, (0–0) S1 17.04 μm, (0–0) S2 12.28 μm, (0–0) S3 9.66 μm) of 3C 236. Based on the flux of the S1, S2 and S3 lines, Dasyra & Combes (2011) computed that the total mass of warm-H$_2$ in 3C 236 is 6.10×10^7 $M_\odot$, with a single excitation temperature of $T = 345$ K. Using the same data set, Guillard et al. (2012) fitted an LTE model of three excitation temperature components to the emission of the warm-H$_2$ in 3C 236. According to their model, the warm-H$_2$ phase is composed of $(1.6 \pm 0.5) \times 10^9$ $M_\odot$ of gas at $T = 100$ K, plus $(9.5 \pm 4.0) \times 10^7$ $M_\odot$ at $T = 241$ K and $7.3 \pm 1.8 \times 10^5$ $M_\odot$ for $T = 1045$ K. The warm-H$_2$ phase is more likely to have a distribution of temperatures, rather than one fixed temperature. Hence, we adopt the Guillard et al. (2012) model in our estimate of the warm-to-cold H$_2$ ratio in 3C 236, for which we obtain a value of 0.81. Gas-rich star-forming galaxies usually present a warm-to-cold H$_2$ ratio of 0.01–0.1 (e.g., Higdon et al. 2006; Roussel et al. 2007). Ogle et al. (2010) showed that this ratio is significantly higher in powerful radio galaxies classified as MOHEGs, where the ratio ranges from ~ 0.2 to ~ 2. The ratio measured in 3C 236 lies within the values found in MOHEGs.

Although the optical line ratios measured in 3C 236 are consistent with those of low-excitation radio AGNs (LERAGN, Smolčić 2009; Hardcastle et al. 2006), the $M(H_2)/M_*$ ratio ($\sim 0.23\%$) and the M_{bh}/M_{sph} ratio ($\sim 0.05\%$) measured in 3C 236 are similar to the values found in high-excitation radio AGNs (HERAGN, Smolčić & Riechers 2011). The mixed properties of 3C 236 could be a consequence of the recent merger-driven reactivation of star formation and AGN activities in this source[4].

5. Evidence of outflow in 3C 236

Based on the HI spectrum of 3C 236 obtained with the WSRT, which shows a 2000 km s^{-1} – wide absorption profile, Morganti et al. (2005) identified in this source an extreme outflow of atomic hydrogen. In the light of the new redshift of the source determined from CO, we discuss below the existence of outflow signatures that can be found from the analysis of the kinematics of different ISM components of 3C 236.

5.1. Cold molecular gas: CO line emission

The kinematics of the spatially resolved CO disk, analyzed in Sect. 4, can be explained by circular rotation around the AGN. Our data do not sample the extreme blueshifted end of the HI outflow (beyond $v - v_{sys}^{CO} < -332$ km s^{-1}). We nevertheless note that the data show no signs of significant emission at the high end represented by extreme *red* velocities (883 km s^{-1} > $v - v_{sys}^{CO} > 368$ km s^{-1}), which are fully covered in our observations. The implied upper limit to the molecular mass of the *red* lobe of the outflow is $\lesssim 4.4 \times 10^8$ $M_\odot$. We used the properties of the molecular outflow of Mrk 231 as an extreme upper limit to what could be expected in 3C 236: if we were to adopt

---

[4] LERAGN are usually hosted by galaxies on their final stages of the mass assembly, with older stellar populations and redder colors compared to their HERAGN counterparts.
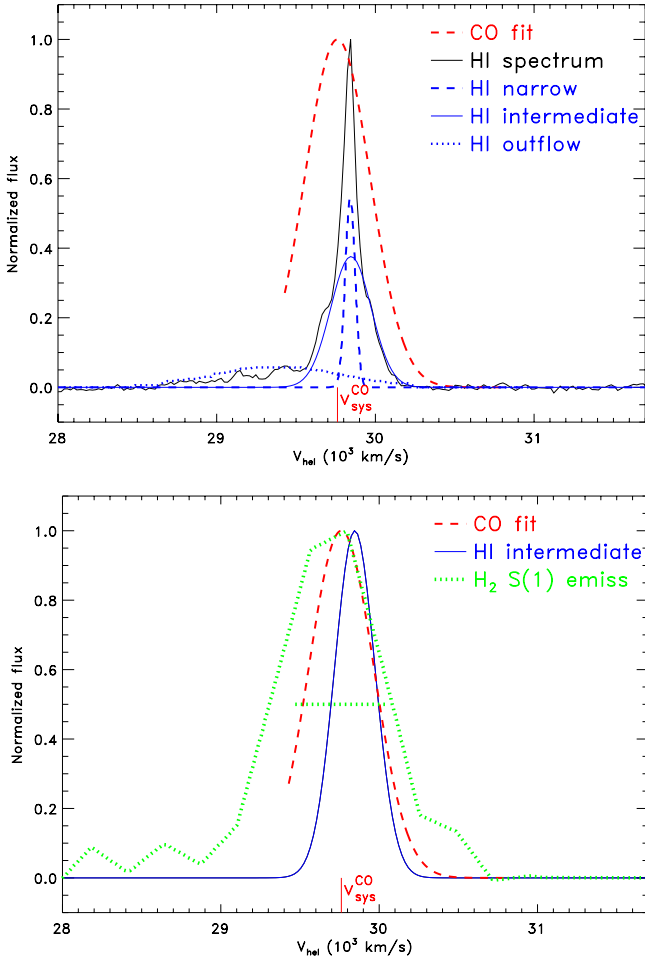
Fig. 6. H I absorption (Morganti et al. 2005), H_2 S(1) 17 μm emission (Dasyra & Combes 2011), and Gaussian fit of the ^{12}CO(2−1) emission of 3C 236. For comparison, the spectra are normalized and the H I absorption is shown inverted. The red vertical line marks the v_{sys}^{CO}. *Top panel*: comparison of the CO emission (red, dashed line) and H I absorption. The black line shows the integrated H I absorption spectrum of 3C 236. The three components of the fit to the H I spectrum are represented with blue lines. *Bottom panel*: comparison of the CO emission (red, dashed line), H_2 S(1) 17 μm emission (green line), and the H I intermediate width component (blue line). The horizontal green line shows the FWHM of the H_2 S(1) 17 μm line, corrected for instrumental broadening.

in 3C 236 the same scaling for the outflow/disk mass ratio measured in Mrk 231 (i.e., $M(H_2)_{outflow}/M(H_2)_{disk} \sim 0.06$, Feruglio et al. 2010; Cicone et al. 2012), the expected H_2 mass in the outflow would amount to 1.2×10^8 $M_\odot$. This is a still factor $\simeq 4$ below the detection limit derived above for 3C 236. We can therefore conclude that the presence of a molecular outflow that would share the extreme properties measured in Mrk 231 would have remained unnoticed in 3C 236 by our observations.

5.2. Atomic gas: HI line absorption

Figure 6 shows the integrated H I absorption profile of 3C 236 (Morganti et al. 2005). The spectrum was inverted for the sake of comparison with the CO emission profile. The H I line profile shows three distinct velocity components hereafter referred to as *narrow*, *intermediate*, and *outflow* components. The *narrow* and *intermediate* components were already detected by van Gorkom et al. (1989) using the VLA. The *outflow*

component has been confirmed with EVLA observations (A array, Morganti et al., in prep.). The velocity centroids and widths derived from the Gaussian fits to the *narrow* and *intermediate* components (*narrow*: v(HEL) = 29 828 km s^{-1}, *FWHM* $\sim$ 80 km s^{-1}; *intermediate*: v(HEL) = 29 846 km s^{-1}, *FWHM* $\sim$ 300 km s^{-1}) differ significantly from the parameters of the *outflow* component (v(HEL) = 29 474 km s^{-1}, *FWHM* $\sim$ 1100 km s^{-1}). As argued below, the H I spectrum can be explained by two kinematically distinct systems: a rotating disk and an outflow.

The main limitation of the Morganti et al. (2005) data, if we are to pinpoint the origin of the different components of the H I spectrum, is their lack of spatial resolution. The comparison between the integrated H I and CO profiles can be used to discuss the possible location of the H I absorbers, however. As shown in Fig. 6, the velocity range covered by the *narrow* and *intermediate* components is similar to the one covered by CO emission. This similarity can be taken as indirect evidence that the deep H I absorption is explained by a rotating H I structure that is likely concomitant with the molecular disk. This would leave out the evidence of H I outflow only to the most extreme velocities (-1000 km s$^{-1} < v - v_{sys}^{CO} < -500$ km s^{-1})[5]. The new VLBI map of 3C 236 presented by Struve & Conway (2012) has recently confirmed this scenario by showing that the H I absorption of the *narrow* and *intermediate* component come from a rotating structure characterized by an orientation almost identical to that of the CO disk. The location of the H I *outflow* remains unknown, however, because the velocity range of the *outflow* lies well beyond the bandwidth covered by the data of Struve & Conway (2012).

5.3. Warm molecular gas: H_2 line emission

Figure 6 (bottom panel) shows the H_2 S(1) emission line profile detected in 3C 236 by Dasyra & Combes (2011)[6]. A comparison of the S(1) line with the Gaussian fit to the ^{12}CO(2−1) spectrum and with the H I *intermediate* component indicates that the line profiles of these tracers are similar (Fig. 6, bottom panel). The velocity centroids and deconvolved widths of the lines are almost identical within the errors ($\Delta v \sim 50$ and 60 km s^{-1} for H I and H_2 centroids, respectively). Even though the apparent FWHM of the S1 line (750 ± 75 km s^{-1}) is $\sim 50\%$ larger compared to the CO line and the H I *intermediate* component, this difference disappears if the instrumental broadening of the S(1) line is taken into account (*FWHM* = 582 ± 60 km s^{-1}, corrected for instrumental broadening). This similarity can be taken as indirect evidence that the warm-H_2 emission of 3C 236 is probably generated in the same rotating disk as the CO emission.

5.4. Ionized gas: optical line emission

Figure 7 shows the optical emission lines H_β and [O III] $\lambda\lambda4959$, 5007 Å of 3C 236, taken from the SDSS archive. The three lines show a remarkable large width, also seen in the optical emission of $H\alpha$, [N II]$\lambda\lambda6548$, 6584 Å, [S II]$\lambda\lambda6713$, 6731 Å lines, as well as in the IR lines [Ne II] and [Ne III] (Dasyra & Combes 2011; Guillard et al. 2012). Figure 8 shows a zoom on the H_β and [O III] $\lambda5007$ Å lines, with the Gaussian fit to the

---

[5] We note that previous claims of an extreme H I outflow in 3C 236 were mainly due to the wrong value assumed for v_{sys}.

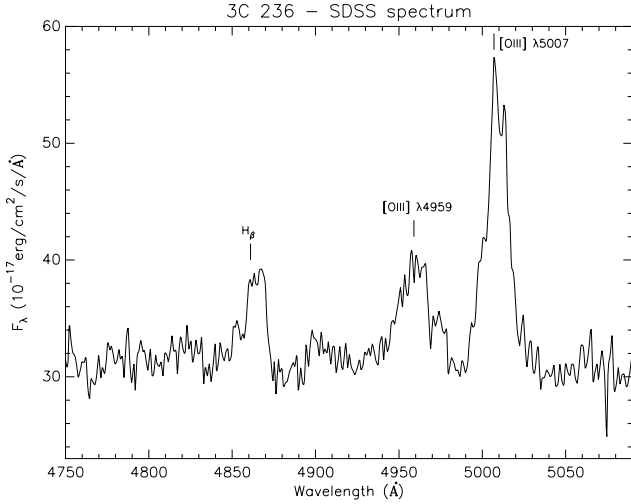[6] The S(1), S(2) and S(3) lines detected in 3C 236 show similar FWHM (Dasyra & Combes 2011).

Fig. 7. Optical rest-frame spectrum of 3C 236 from SDSS (z_{SDSS} = 0.0991). For clarity, we only show the region of the Hβ and [O III]$\lambda\lambda$4959, 5007 Å emission lines.
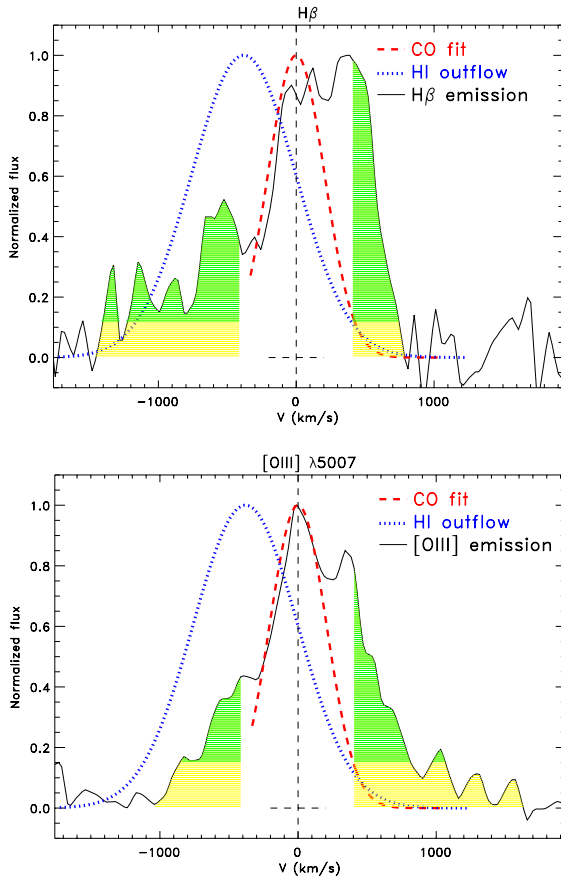

Fig. 8. Zooms of the Hβ (*top panel*) and [O III]λ5007 Å (*bottom panel*) emission lines (black, solid line), with the ^{12}CO(2−1) emission (red, dashed line), and H I outflow absorption (blue, dotted line) overlaid. For comparison, all fluxes are normalized and the H I absorption is inverted. The horizontal dashed line shows the FWHM of ^{12}CO(2−1) emission. The vertical dashed line marks the v_{sys}^{CO}. The shaded areas mark the emission of the optical lines beyond ±400 km s^{-1}, above the continuum (yellow) and 3σ (green) levels. (Color version available in electronic format.)

^{12}CO(2−1) spectrum and the H I *outflow* component overlaid. This figure shows that a sizable fraction of the total emission of the lines (above 3σ-levels) is detected at extreme red

and blue velocities: $|v−v_{sys}^{CO}| > 400$ km s^{-1}, i.e., well beyond the range allowed by the rotation of the disk (see discussion in Sect. 4). While the velocity centroids of the optical lines are similar to v_{sys}^{CO}, their widths (*FWHM* ~ 900 km s^{-1}, *FWZI* ~ 2000 km s^{-1}) are ~3 times the value measured for the ^{12}CO(2−1) line.

The imprint of the outflow is clearly detected on the red and the blue wings of the optical lines, suggesting that, unlike the emission from the star-forming disk, the emission from the outflowing gas is not as heavily extincted (see discussion in Sect. 6.1.1). The similar FWZI of the line wings suggests that the red wing is produced in the receding side of the same outflow system. The lack of spatial resolution prevents us from clearly identifying the origin of the outflow, however. A comparison with the H I outflow component shows that the blue wing of the ionized gas emission lines covers a comparable velocity range, which suggests that the ionized gas outflow may have started to recombine and form H I (e.g., Morganti et al. 2003b).

6. Star-formation properties of 3C 236

Nesvadba et al. (2010) studied the relation between the SFR surface density and the molecular gas surface density derived from CO in a sample of radio galaxies. The SFR was estimated based on the 7.7 μm PAH feature emission, except for 3C 326 N, where the 70 μm continuum emission was also used as an SFR tracer (Ogle et al. 2007). With all the caveats discussed by Nesvadba et al. (2010) in mind, an inspection of the Kennicut-Schmidt (KS) law shown in Fig. 9 of their paper indicates that powerful radio sources are systematically associated with PAH intensities that are a factor ~10–50 lower than normal galaxies for a given mass. This offset is suggestive of a lower star-formation efficiency ($SFE = SFR/M(H_2)$) in MOHEGs compared to normal galaxies.

Nesvadba et al. (2010) pointed to the influence of large-scale shocks as the agent responsible for increasing the turbulence of molecular gas (see also Nesvadba et al. 2011). This energy injection into the medium could inhibit star formation to a large extent. In Sect 6.2, we study the SFE and the location of 3C 236 in the KS diagram, and discuss the differences with respect to the results obtained by Nesvadba et al. (2010) in their sample of MOHEGs. To this aim we used several tracers of the SFR available for 3C 236 (discussed in Sect 6.1). This is required if we are to constrain the potential biases inherent to the different SFR calibrations. Some SFR tracers are sensitive to the presence of AGN radiation and jet-induced shocks in the ISM, as these may increase the flux of ionized gas emission lines, vary the shape of the continuum, and destroy ISM molecules like the PAH. A possible evolutionary scenario explaining the differences between the samples is discussed in Sect. 6.3.

6.1. Star-formation rate estimations

6.1.1. Optical/ultraviolet photometry

Tremblay et al. (2010) and O'Dea et al. (2001) used HST high-resolution imaging in the FUV, NUV, *U*, and *V* bands to study the star formation in 3C 236 (see also Baldi & Capetti 2008). As illustrated in Fig. 9, the FUV emission consists of five knots distributed in the inner 4.5 kpc of 3C 236: there is one central knot located at the AGN and four knots arranged in an arc along the outer edge of the inner dusty disk described in Sect. 4. Tremblay et al. (2010) concluded that all knots are associated with star-formation episodes but of significantly
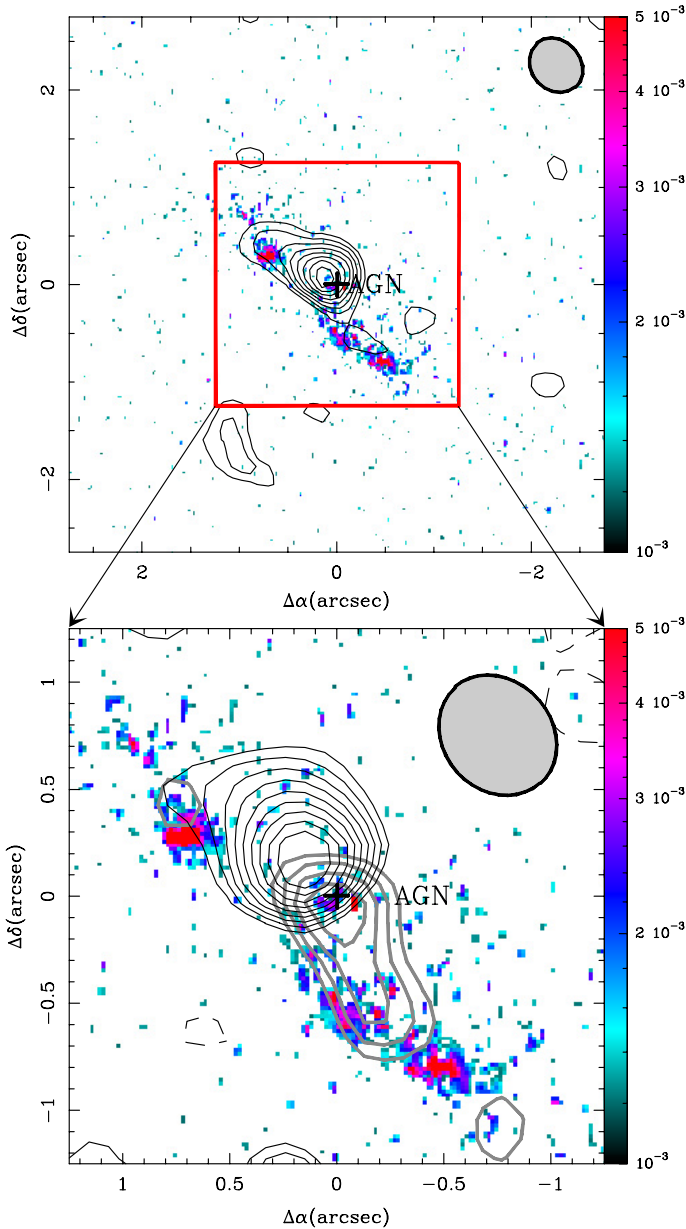
Fig. 9. *Top panel*: HST FUV image of the star forming regions of 3C 236, with the integrated ^{12}CO(2−1) emission overlaid. *Bottom panel*: zoom into the central 3″ of 3C 236. The contours correspond to the ^{12}CO(2−1) emission integrated in the red (thin, black line) and blue (thick, gray line) channels. Contour levels as in Fig. 4. HST image in counts s^{-1}. (Color version available in electronic format.)

in the inner disk and, thus, the SFR estimate of Tremblay et al. (2010) is probably a lower limit of the total SFR of 3C 236. The emission detected in the UV knots observed would arise from the outermost, low-extinction layers of the inner dust disk.

The extinction of the inner dust disk does not seem to significantly absorb the emission of the ionized gas outflow, which shows both red and blue wings in the spectrum (Sect. 5.4). Based on the emission line fluxes from the SDSS spectrum of 3C 236, the Cardelli et al. (1989) extinction law yields significantly lower extinction values: $A_V = 1.4$ (using $E(B − V) = 0.456$, Tremblay et al. 2010). This suggests that the outflow is formed in a different region of 3C 236, probably the compact nucleus, which is visible in the UV images. High-resolution spectroscopy would be needed to identify the location of the outflow.

The UV and optical emission of powerful radio galaxies may have a significant contribution from the AGN. This may cause a severe overestimation of the SFR if this contribution is not deducted. Tremblay et al. (2010) discussed that the contribution from emission lines to their UV and optical bands is negligible for 3C 236, however. A similar conclusion was reached by Holt et al. (2007), who fitted the shape of the continuum emission subjacent to the optical spectrum of 3C 236 inside the range 3000–7000 Å. In their analysis, Holt et al. (2007) found no evidence of a significant AGN component.

Some CSS sources are known to show UV nebulosities that are roughly co-spatial with the region occupied by the expanding radio jet (Labiano et al. 2008). This association suggests that both emission features are related in these sources. In the case of 3C 236 however, the radio jets are perpendicular to the star-forming disk revealed by the HST images. This different geometry indicates that the UV and optical knots are mostly unrelated to the jet lobes in this source. We can therefore conclude that the UV and optical emission from the star-forming regions of 3C 236 has a negligible contribution from the AGN. The value derived for the SFR (7.51 $M_\odot$ yr^{-1}) from these tracers is in all likelihood not significantly biased.

6.1.2. Optical spectroscopy

The Hα emission of a galaxy is indicative of its SFR (Kennicutt 1998). Using the Hα line flux from SDSS ($F_{H\alpha} = 5.62 \times 10^{-15}$ erg s^{-1} cm^{-2}, Buttiglione et al. 2009), and the Hα-SFR relationships of Kennicutt (1998), we obtain an $SFR = 1.1$ $M_\odot$ yr^{-1} for 3C 236. If a galaxy harbors an AGN, the nuclear activity can alter the Hα flux through photoionization and/or shocks. To estimate the contributions from the AGN to the Hα emission, we used the so-called diagnostic diagrams or Baldwin-Phillips-Terlevich (BPT) diagrams (Baldwin et al. 1981; Veilleux & Osterbrock 1987). Buttiglione et al. (2009) measured the de-reddened ratios of the optical emission lines in the SDSS spectrum of 3C 236. A comparison of the values of [O III]/Hβ, [N II]/Hα, [S II]/Hα, and [O I]/Hα from Buttiglione et al. (2009) with the results of Kewley et al. (2001) and Brinchmann et al. (2004) shows that the contribution of the AGN to the Hα flux of 3C 236 is $\lesssim 10\%$. Removing 10% of the flux of the Hα line yields an $SFR = 1.0$ $M_\odot$ yr. Based on the same BPT diagrams, we find that the optical line ratios of 3C 236 are also compatible with ionization from shocks with velocities $\lesssim 300$ km s^{-1}. These shocks could be generated either by the AGN or by star formation processes.

The 4000 Å break (D4000, Balogh et al. 1999) is indicative of the SFR per unit of stellar mass (M_*) in AGN (Brinchmann et al. 2004). For 3C 236, D4000 $\simeq 1.8$ (Holt et al. 2007),

different ages: $\sim 10^9$ yr for the nucleus, and $\sim 10^7$ yr for the arc. Using Starburst99 stellar population synthesis models to fit the data, Tremblay et al. (2010) determined that the UV-derived SFR of 3C 236 is 7.51 $M_\odot$ yr^{-1}.

Figure 9 shows that the star-forming regions of 3C 236 lie on the nearest edge of the CO and inner dust disk, while the rest of the galaxy shows no UV emission (except for the compact nucleus). This morphology, strongly asymmetrical with respect to the galaxy major axis, suggests that there is a strong extinction in the inner dust disk. If we calculate the extinction using the $N(H)$ values derived from CO and X-ray data (Sect. 4.3), the Bohlin et al. (1978) relationships yield $A_V = 10$ and $A_V = 50$. Therefore, the UV images of 3C 236 are probably missing UV emission from the star forming regions embedded

which yields $SFR/M_* \sim 1 \times 10^{-11}$–$10^{-12}$ yr^{-1}. Using the total stellar mass of 3C 236 estimated by Tadhunter et al. (2011), $M_* = 10^{12}\ M_\odot$, we obtain $SFR \sim 1$–$10\ M_\odot$ yr^{-1}, consistent with the SFR estimations of Sect. 6.1.1.

6.1.3. Mid-infrared continuum

Calzetti et al. (2007) presented two SFR calibrations for their sample of nearby galaxies, one using the 24 μm luminosity of the source, the other combining the 24 μm and Hα luminosities (see also Kennicutt et al. 2009). Applying these calibrations to the 24 μm emission ($F_{24\ \mu m} = 2.16 \times 10^{-12}$ erg s^{-1} cm^{-2}, Dicken et al. 2010), and the Hα emission (Sect. 6.1.2) of 3C 236, we obtain an $SFR = 6.62\ M_\odot$ yr^{-1} and an $SFR = 9.63 \pm 1.7\ M_\odot$ yr^{-1}.

Dicken et al. (2010) also measured the 70 μm flux of 3C 236 with *Spitzer*: $F_{70\ \mu m} = 2.77 \times 10^{-12}$ erg s^{-1} cm^{-2}. Based on the 70 μm emission, we can establish a lower and upper limit (Dicken 2011, private communication; see also Seymour et al. 2011) on the SFR of 3C 236: $3\ M_\odot$ yr$^{-1} \lesssim SFR \lesssim 10\ M_\odot$ yr^{-1}.

The 24 μm and 70 μm emission can be increased by the heating of dust by the AGN (Tadhunter et al. 2007), producing an overestimated SFR. However, Dicken et al. (2010) found that the 70 μm emission of 3C 236 is ∼9 times higher than expected for a non-starburst galaxy with the same [O III] luminosity. This authors argued that this difference is attributable to star formation being the main contributor to the 70 μm flux. The SFR derived from the 24 μm and 70 μm are consistent with the SFR derived in Sect. 6.1.1, suggesting that the contribution from the AGN to these fluxes is low, and the SFR estimations from the IR continuum are accurate.

6.1.4. Mid-infrared spectroscopy

Willett et al. (2010) used the [Ne III]λ15.6 μm and [Ne II]λ12.8 μm fluxes to measure the SFR in a sample of compact symmetric objects (CSO, see also Ho & Keto 2007). The neon emission lines of 3C 236 have fluxes $F_{[Ne\ II]} = (0.92 \pm 0.06) \times 10^{10}$ erg s^{-1} cm^{-2} and $F_{[Ne\ III]} = (0.44 \pm 0.03) \times 10^{10}$ erg s^{-1} cm^{-2} (*Spitzer* spectrum, Guillard et al. 2012), which yield an $SFR = 16 \pm 1\ M_\odot$ yr^{-1}.

To assess the AGN contribution to the total MIR luminosity of a galaxy, Willett et al. (2010) compared the [O IV]λ25.9 μm/[Ne II] λ12.8 μm ratio with the equivalent width of the 6.2 μm PAH emission. We measured [O IV]/[Ne II] < 0.2 and, $EW_{6.2} < 170\ \mu$m (3σ limit) from the *Spitzer* spectrum of 3C 236. Hence, the AGN contribution in 3C 236 is <10%. Genzel et al. (1998) used the 7.7 μm PAH strength, instead of the 6.2 μm, to study the contribution of the AGN to the galaxies in their sample. If we consider the 7.7 μm PAH strength of 3C 236, the contribution from the AGN is ≲20%, consistent with the samples of *star-formation dominated* galaxies (Genzel et al. 1998). Assuming that the AGN contributes in the same proportion to the MIR luminosity and the neon lines, removing 20% of the neon lines flux yields an $SFR = 12.9 \pm 0.5\ M_\odot$ yr^{-1}.

Another indication of the AGN contribution is given by the ratio [Ne III]/[Ne II], which increases with the hardness of the ionizing environment. For 3C 236, log [Ne III]/[Ne II] = −0.3, similar to the mean value of the ratio in ULIRG and starburst galaxies (−0.35), and below the mean value for AGN (−0.07) and CSO (−0.16, Willett et al. 2010), suggesting a low contribution from the AGN in 3C 236.

Pereira-Santaella et al. (2010) published a list of IR emission line ratios for their sample of 426 active and HII galaxies.

Based on their results, the [O IV]/[Ne II] and [Ne III]/[Ne II] ratios of 3C 236 are closer to the values observed in LINER-like and HII galaxies rather than in Seyferts or quasi-stellar objects. Therefore, the SFR of 3C 236, obtained with IR line ratios, is not largely overestimated due to AGN effects. It is also consistent with the SFR values derived in Sect. 6.1.1.

6.1.5. PAH emission

The *Spitzer* spectrum of 3C 236 shows that the emission of the PAH features is $F_{11\ \mu m} = 3.7 \times 10^{-14}$ erg s^{-1} cm^{-2}, $F_{7.7\ \mu m} < 6.8 \times 10^{-14}$ erg s^{-1} cm^{-2}, and $F_{6.3\ \mu m} < 3.8 \times 10^{-14}$ erg s^{-1} cm^{-2} (3σ limits, Dicken et al. 2012; Guillard et al. 2012).

Based on the 7.7 μm PAH emission limit, we used the Calzetti et al. (2007) equations (see also, Nesvadba et al. 2010) to establish a 3σ-limit on the SFR of 3C 236: $SFR \lesssim 0.23\ M_\odot$ yr^{-1}. This upper limit falls below any other SFR estimation for 3C 236, and is consistent with the SFR (which was also calculated using the 7.7 μm emission) of the Nesvadba et al. (2010) radio galaxies with H$_2$ masses ∼$10^9\ M_\odot$.

Willett et al. (2010) used a second method to calculate the SFR in their sample, based on the correlation found between the neon emission line luminosities and the 6.2 μm plus 11.3 μm PAH luminosities (see also Farrah et al. 2007). For 3C 236, the total flux of the 6.2 μm and 11.3 μm PAH emission is 3.7×10^{-14} erg s^{-1} cm$^{-2} < F_{6.2\ \mu m} + F_{11.3\ \mu m} < 7.5 \times 10^{-14}$ erg s^{-1} cm^{-2}, yielding $11\ M_\odot$ yr$^{-1} \lesssim SFR \lesssim 22\ M_\odot$ yr^{-1}. Leaving aside the estimate derived from the 7.7 μm PAH feature, we conclude that the average value of the SFR obtained from all the different tracers discussed above is $SFR \sim 9.2\ M_\odot$ yr^{-1} (the corresponding value from the 7.7 μm emission is thirty-five times lower). It is thus tempting to speculate that 7.7 μm emission underestimates the SFR in 3C 236.

O'Dowd et al. (2009) found that sources with an AGN component have weaker 7.7 μm emission than quiescent galaxies, consistent with the destruction of smaller PAH by shocks and/or radiation from the AGN. Modeling the PAH interactions with the ISM shows that PAH are destroyed by shocks with velocities ≳125 km s^{-1} (Micelotta et al. 2010a,b, and references therein). The shock velocities measured in the warm-H$_2$ phase of 3C 236 are too small (≲30 km s^{-1}, Guillard et al. 2012), however, to destroy the PAH[7]. Another mechanism of PAH destruction is by the AGN radiation field. Hard-UV and X-rays will destroy PAH at kiloparsec distances from the AGN (e.g., Siebenmorgen et al. 2004; Voit 1992). As discussed above, the star-forming knots in 3C 236 are not found to be contaminated by the effects of AGN radiation, however. Similarly, the PAH destruction from hard-UV and X-rays should in all likelihood affect only the nuclear region, leaving aside the star-forming knots far from the AGN. The reasons behind the discrepancy between the SFR value derived from the 7.7 μm PAH and the remaining tracers in 3C 236 remain therefore unknown.

6.2. Star-formation efficiency in 3C 236: normal or inhibited?

Figure 10 shows the SFR surface density ($\Sigma_{SFR} = SFR/area$) and cold-H$_2$ mass surface density ($\Sigma_{MH2} = M(H_2)/area$) for 3C 236

---

[7] PAH emission is likely produced in the PDR-like phase of molecular gas at temperatures ≥100 K, which is also the major contributor to the bulk of H$_2$ line emission.
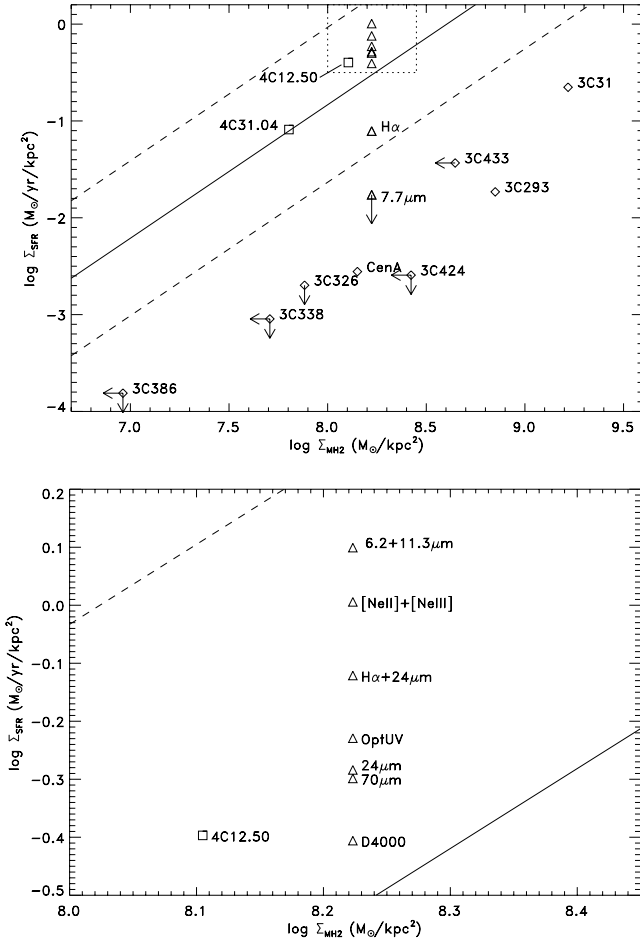
Fig. 10. Σ_{SFR} and Σ_{MH2} of 3C 236 (triangles), the Nesvadba et al. (2010) sample (diamonds), and young sources 4C 12.50 and 4C 31.04 (squares). The *bottom panel* is a zoom on the area marked with a dotted box, into which most of the SFR estimates of 3C 236 fall. Solid line: best-fit of the KS law from Kennicutt (1998). Dashed lines: dispersion around the KS law best fit for normal star-forming galaxies (Roussel et al. 2007; Kennicutt 1998).

and the Nesvadba et al. (2010) sample[8]. It also shows the canonical KS-law fitted for normal star-forming galaxies (Roussel et al. 2007; Kennicutt 1998). For the surface density calculations, we assumed that the entire star formation of 3C 236 is produced in a disk of radius $R = 1.1''$ (deprojected area 12.7 kpc^2), which includes the molecular gas disk, and all UV emission from the star-forming knots. Table 2 lists all SFR estimates for 3C 236, the areas considered, and the corresponding cold-H$_2$ mass.

Figure 10 shows that the Σ_{SFR} of 3C 236 is consistent with the Σ_{SFR} of normal star-forming galaxies at similar Σ_{MH2}. In terms of SFE, 3C 236 shows $SFE_{3C236} = 4$ Gyr^{-1}. For a normal galaxy with the same Σ_{MH2} as 3C 236, the KS law yields $\Sigma_{SFR} = 0.33\ M_\odot$ yr^{-1} kpc^{-2}. Therefore, the implied $SFE_{normal} = 2$ Gyr^{-1}. For the Nesvadba et al. (2010) sample, the SFE (0.02–0.04 Gyr^{-1}) is 10–50 times lower than measured in normal galaxies. Compared to the powerful radio galaxies of Nesvadba et al. (2010), 3C 236 is an efficient star-forming radio galaxy. At

---

[8] The data available from Nesvadba et al. (2010) do not include warm-H$_2$. Therefore, we considered only the cold-H$_2$ mass for the comparison of star-formation laws, which yields log $\Sigma_{MH2} \simeq 8.2\ M_\odot$ kpc^{-2}. Adding the cold and warm-H$_2$ masses of 3C 236 yields log $\Sigma_{MH2} \simeq 8.5\ M_\odot$ kpc^{-2}.

Table 2. Star-formation rates estimates of 3C 236.

Region	Tracer	SFR ($M_\odot$ yr^{-1})	$M(H_2)$ ($10^8\ M_\odot$)	Area (kpc^2)	Refs.
All	Optical+UV	7.51	21.3	12.7	1
Unresolved	Hα	1.0	21.3	12.7	2,3
Unresolved	D4000	1–10	21.3	12.7	4,5
Unresolved	24 μm	6.62	21.3	12.7	6,7
Unresolved	24 μm+Hα	9.63 ± 1.7	21.3	12.7	2,6,7
Unresolved	70 μm	3–10	21.3	12.7	6,8
Unresolved	7.7 μm	<0.24	21.3	12.7	7,9
Unresolved	6.2+11.3 μm	11–22	21.3	12.7	10,11
Unresolved	[Ne II]+[Ne III]	12.9 ± 0.5	21.3	12.7	10,11
Region 0	FUV	6.19	21.3	12.7	A
Region 1	FUV	0.84	<9.93	3.0	A
Region 2	FUV	1.43	5.49	2.4	A
Region 3	FUV	1.27	4.93	2.5	A
Region 4	FUV	1.48	3.66	2.5	A
Region 5	FUV	1.17	<12.5	2.3	A

Notes. Limits are 3σ. Uncertainties in $M(H_2)$ are ~5%. SFR uncertainties listed when available.
References. 1-Tremblay et al. (2010), 2-Buttiglione et al. (2009), 3-Kennicutt (1998), 4-Holt et al. (2007), 5-Brinchmann et al. (2004), 6-Dicken et al. (2010), 7-Calzetti et al. (2007), 8-Seymour et al. (2011), 9-Guillard et al. (2012), 10-Dicken et al. (2012), 11-Willett et al. (2010), A-Appendix A of this work.

the current rate, 3C 236 will deplete its H$_2$ gas in $t_{deplete} \sim 2$ Gyr. Our SFR calculations do not consider the extincted star-forming regions embedded in the inner dust disk (Sect. 6.1.1). The inclusion of these regions in the SFR estimations would increase the SFE value of 3C 236 and thus the difference with the radio galaxies of Nesvadba et al. (2010).

The HST images and CO map of 3C 236 provide enough resolution to study the spatial distribution of the SFE. In Appendix A, we discuss how the Σ_{SFR} and Σ_{MH2} change along the molecular gas disk of 3C 236. Our analysis shows that all star-forming regions of 3C 236 have an SFE consistent with the KS law of normal galaxies. The source 3C 236 shows a high global SFE compared with other radio galaxies. This property cannot be attributed to any particular location in the disk.

6.3. AGN feedback in radio-galaxies: an evolutionary path?

The source 3C 236 has undergone two epochs of AGN activity, with a phase of inactivity in between of about 10^7 yr. After this dormant phase, an accretion event (e.g., a minor merger[9] or re-settlement of the gas) increased the amount of gas, reactivated the star formation and triggered the (~10^5 yr old) CSS source (Tremblay et al. 2010; O'Dea et al. 2001). With the AGN inactive at the time of the accretion event, the lack of large-scale radio jets and the lobes disconnected to the core, the feedback effects of the old radio source could not affect the newly acquired gas. If an outflow was created at the time of the CSS ignition, it would have needed to travel at an average velocity of 20 000 km s^{-1} to reach the star-forming knots seen in the UV images (located at ~2 kpc from the nucleus) in 10^5 years. This speed is ~10–20 times higher than the fastest outflows observed in radio galaxies. This scenario can therefore be excluded. The molecular gas in the knots has thus not been affected by the CSS source feedback. Therefore, the knots form stars at a

---

[9] O'Dea et al. (2001) detected a small companion galaxy at 10'' from the nucleus of 3C 236.

normal rate. Within 10^6–10^7 yr, the feedback effects may nevertheless reach the knots and inhibit the star formation, lowering the SFE to the values measured for the Nesvadba et al. (2010) radio sources (which have ages of 10^7–10^8 years).

In the scenario described above, where the effects of AGN feedback are closely related to the age of the radio source, we may expect to measure SFE values typical of normal star-forming galaxies in the hosts of other young radio sources. Willett et al. (2010) measured the SFR of nine young sources using the 6.2 and 11.3 μm PAH emission (as shown in Sect. 6.1.5 for 3C 236) and obtained values from 0.8 to 47.8 $M_\odot$ yr^{-1}. Two of these have published cold H$_2$ mass estimations: 4C 12.50 ($SFR = 31.5\ M_\odot$ yr^{-1}, $M(H_2) = (1.0 \pm 0.3) \times 10^{10}\ M_\odot$, Dasyra & Combes 2012) and 4C 31.04 ($SFR = 6.4\ M_\odot$ yr^{-1}, $M(H_2) = 0.5 \times 10^{10}\ M_\odot$, García-Burillo et al. 2007). Figure 10 shows that the SFE of both sources are comparable to the SFE of 3C 236 and thus consistent with the KS-law of normal galaxies. Although the data are scarce, young radio galaxies seem to have a higher SFE than old radio galaxies.

Even though the detection of H I and ionized gas outflows confirms the presence of AGN feedback in the host galaxies of young radio sources, such as those examined in this work, the kinematics of the cold molecular gas and the SFE of the hosts seem mildly affected, however. It is possible that, because of the extreme youth of the AGN, the effects of feedback in young sources have not had the time to propagate to such large scales as in the evolved radio sources.

7. Summary and conclusions

We have used the IRAM PdBI to study the distribution and kinematics of molecular gas of the nearby ($z \sim 0.1$) FR II radio galaxy 3C 236 by imaging the emission of the 2–1 line of ^{12}CO in the circumnuclear region of the galaxy with high spatial resolution (0.6″). The AGN activity has recently been ($\sim 10^5$ yr ago) re-activated in 3C 236, triggered by a merger episode (that occurred $\sim 10^7$ yr ago). Previous observations identified in 3C 236 one of the most extreme H I outflows thus far discovered in a radio galaxy. The new observations presented in this paper were analyzed to search for the footprints of AGN feedback on the molecular ISM of 3C 236. In particular, we looked for evidence of outflow motions in the molecular gas kinematics. Furthermore, we derived the SFE of molecular gas in 3C 236 and compared this value with the SFE obtained in different populations of radio galaxies, including young and evolved radio sources. We investigated if the star-formation properties of 3C 236 deviate from the KS relation followed by normal star-forming galaxies.

We summarize below the main results and conclusions of this work:

- The CO emission comes from a spatially resolved 2.6 kpc-diameter disk that has a gas mass $M(H_2) = 2.1 \times 10^9\ M_\odot$. The CO disk is linked to the inner region of a highly inclined dusty disk identified in the V–H HST color image of the galaxy. The molecular disk is fueling a star-formation episode singled out by a chain of strong emission knots detected at UV wavelengths in the HST pictures of 3C 236.
- The kinematics of the CO disk are dominated by circular rotation and show no indications of high-velocities attributable to outflows. However, based on the limits imposed by the sensitivity and velocity coverage of our data, we cannot exclude a molecular gas outflow in 3C 236 comparable to the one detected in Mrk 231. The gas disk rotates regularly around the AGN core. The latter is identified by prominent radio continuum emission detected at 3 mm and 1 mm wavelengths in our map. Based on the observed CO kinematics we determined an upper limit for the redshift of the source $z_{CO} = 0.09927 \pm 0.0002$ ($v_{sys}^{CO} = 29\,761 \pm 40$ km s^{-1}). The new value of v_{sys} is significantly blueshifted (>350 km s^{-1}) with respect to the value of the systemic velocity previously reported in the literature for the source.
- In the light of the new redshift value, the bulk of the deep H I absorption can be simply explained by a rotating H I structure, leaving out the evidence of outflow only to the most extreme velocities (–1000 km s^{-1} < $v - v_{sys}^{CO}$ < –500 km s^{-1}). Outflow signatures from the CO emitting gas are also absent in the warm molecular gas emission traced by infrared H$_2$ lines. Nevertheless, a reanalysis of the ionized gas kinematics revealed a fast outflow visible in the high-velocity (~ 1000 km s^{-1}) blue- and redshifted line emission wings.
- We derived the SFR of 3C 236 using the different tracers available at optical, UV and MIR wavelengths. The most reliable SFR value comes from high-resolution UV-optical photometry, which in 3C 236 seems mostly unaffected by AGN contribution. Most of the other SFR tracers examined may have contributions from the AGN, however. The consistency of the SFR values obtained with all SFR tracers suggests nevertheless that the AGN contribution is kept low. High-resolution spectroscopy of the UV star-forming knots would be needed to accurately measure the AGN contribution.
- The SFE of the molecular disk, defined as $SFE = SFR/M_{gas}$, is fully consistent with the value measured in normal galaxies, i.e., systems that form stars following the canonical KS law. This result is at odds with the values that are lower by factor of 10–50 that have been claimed to characterize the SFE of evolved powerful radio galaxies. As an explanation for the different SFE measured in young and evolved radio sources, the most likely scenario in 3C 236 suggests that none of the effects of AGN feedback have yet had the time to affect the kinematics or the SF properties of the molecular ISM due to the extreme youth of the AGN re-activation episode in this source.

This simple evolutionary scenario remains to be confirmed using larger samples, and most notably, using different tracers of the SFR in radio galaxies. As a caveat, we point out that most of the estimates of the SFR in evolved radio sources have thus far been derived from the strength of the PAH bands at 7.7 μm. The *low* SFR values in these sources may be severely underestimated due to the destruction of PAH carriers by shocks and/or strong UV and X-ray fields; these ingredients are known to be in place particularly in radio-loud AGN. The reported differences in the SFE of young and evolved radio galaxies could simply reflect a mismatch in the calibration of the SFR tracers used.
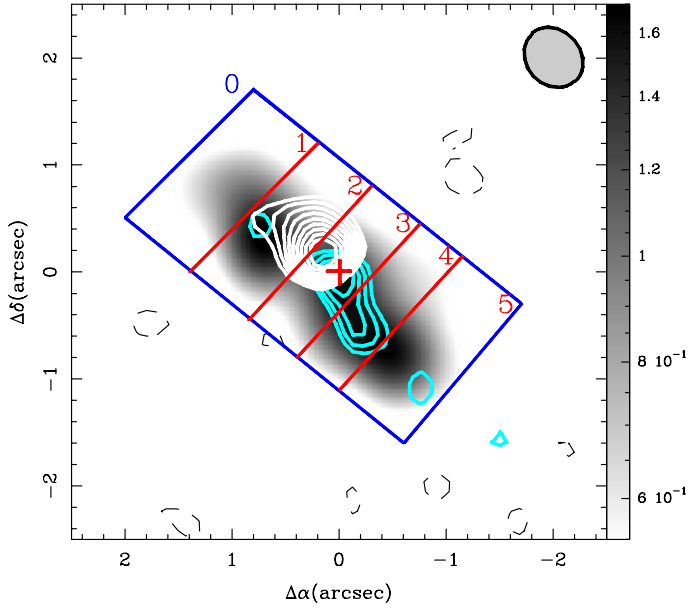
Fig. A.1. HST FUV image of the star-forming regions of 3C 236, smoothed with the beam of CO, with the red and blue ^{12}CO(2−1) channels overlaid. Contour levels as in Fig. 4. Rectangles show the schematic location of the different regions for the analysis of the SFR and H$_2$ distribution. (Color version available in electronic format.)

Appendix A: Spatially resolved SFE of 3C 236

The emission of the star-forming regions and the CO of 3C 236 are almost co-spatial, suggesting that 3C 236 is using the cold molecular gas traced by CO to form stars. The resolution of the HST images and the CO map are sufficient to study the SFE along the molecular gas disk of 3C 236. Therefore, we searched for the star-forming region responsible for the normal (KS law) SFE of 3C 236.

Firstly, we smoothed the HST FUV image with the beam of the ^{12}CO(2−1) maps to have the same resolution in both images. We then divided the disk into five regions, based on the UV emission and molecular gas content. Figure A.1 shows the smoothed FUV image with the ^{12}CO(2−1) blue and red channels overlaid, and the location of the five regions. Regions 1 and 5 correspond to the most external UV emission with no ^{12}CO(2−1) detection above 3σ levels. Regions 2 and 4 have UV and ^{12}CO(2−1) emission. Region 3 corresponds to the center of the disk. Region 0 is the sum of regions 1 through 5.

The $SFR = 7.51\ M_\odot\ \mathrm{yr}^{-1}$ was calculated using the entire flux down to 1σ over the background (aperture "All", Tremblay et al. 2010). To obtain the local SFR for each region, we divided 7.51 $M_\odot\ \mathrm{yr}^{-1}$ by the flux in the "All" aperture and multiplied by the flux of each region. The H$_2$ masses were measured for each region individually, using the ^{12}CO(2−1) emission map. The SFR and H$_2$ contents for each region are listed in Table 2. The SFE of the star-forming regions are $SFE_{R1} > 0.8\ \mathrm{Gyr}^{-1}$, $SFE_{R2} = 3\ \mathrm{Gyr}^{-1}$, $SFE_{R3} = 3\ \mathrm{Gyr}^{-1}$, $SFE_{R4} = 4\ \mathrm{Gyr}^{-1}$, and $SFE_{R5} > 0.9\ \mathrm{Gyr}^{-1}$, consistent with the SFE calculated using the "All" aperture, and the SFE of galaxies following the KS law (e.g., SINGS sample, Kennicutt et al. 2003; Roussel et al. 2007). The SFE of 3C 236 is not a local effect from one individual region; 3C 236 shows a normal SFE all along its molecular gas disk.

References

Aalto, S., Garcia-Burillo, S., Muller, S., et al. 2012, A&A, 537, A44
Abazajian, K. N., Adelman-McCarthy, J. K., Agüeros, M. A., et al. 2009, ApJS, 182, 543
Allen, M. G., Sparks, W. B., Koekemoer, A., et al. 2002, ApJS, 139, 411
Baldi, R. D., & Capetti, A. 2008, A&A, 489, 989
Baldwin, J. A., Phillips, M. M., & Terlevich, R. 1981, PASP, 93, 5
Balogh, M. L., Morris, S. L., Yee, H. K. C., Carlberg, R. G., & Ellingson, E. 1999, ApJ, 527, 54
Barthel, P. D., Miley, G. K., Jagers, W. J., Schilizzi, R. T., & Strom, R. G. 1985, A&A, 148, 243
Best, P. N., Kaiser, C. R., Heckman, T. M., & Kauffmann, G. 2006, MNRAS, 368, L67
Bîrzan, L., Rafferty, D. A., McNamara, B. R., Wise, M. W., & Nulsen, P. E. J. 2004, ApJ, 607, 800
Bohlin, R. C., Savage, B. D., & Drake, J. F. 1978, ApJ, 224, 132
Brinchmann, J., Charlot, S., White, S. D. M., et al. 2004, MNRAS, 351, 1151
Buttiglione, S., Capetti, A., Celotti, A., et al. 2009, A&A, 495, 1033
Calzetti, D., Kennicutt, R. C., Engelbracht, C. W., et al. 2007, ApJ, 666, 870
Cardelli, J. A., Clayton, G. C., & Mathis, J. S. 1989, ApJ, 345, 245
Cicone, C., Feruglio, C., Maiolino, R., et al. 2012, A&A, 543, A99
Ciotti, L., & Ostriker, J. P. 2007, ApJ, 665, 1038
Crenshaw, D. M., Schmitt, H. R., Kraemer, S. B., Mushotzky, R. F., & Dunn, J. P. 2010, ApJ, 708, 419
Crocker, A., Krips, M., Bureau, M., et al. 2012, MNRAS, 421, 1298
Croton, D. J., Springel, V., White, S. D. M., et al. 2006, MNRAS, 365, 11
Dasyra, K. M., & Combes, F. 2011, A&A, 533, L10
Dasyra, K. M., & Combes, F. 2012, ArXiv e-prints
de Koff, S., Baum, S. A., Sparks, W. B., et al. 1996, ApJS, 107, 621
de Koff, S., Best, P., Baum, S. A., et al. 2000, ApJS, 129, 33
Di Matteo, T., Springel, V., & Hernquist, L. 2005, Nature, 433, 604
Dicken, D., Tadhunter, C., Axon, D., et al. 2010, ApJ, 722, 1333
Dicken, D., Tadhunter, C., Axon, D., et al. 2012, ApJ, 745, 172
Fabian, A. C., Celotti, A., & Erlund, M. C. 2006, MNRAS, 373, L16
Fanaroff, B. L., & Riley, J. M. 1974, MNRAS, 167, 31P
Farrah, D., Bernard-Salas, J., Spoon, H. W. W., et al. 2007, ApJ, 667, 149
Feruglio, C., Maiolino, R., Piconcelli, E., et al. 2010, A&A, 518, L155
Fischer, T. C., Crenshaw, D. M., Kraemer, S. B., et al. 2011, ApJ, 727, 71
Floyd, D. J. E., Axon, D., Baum, S., et al. 2008, ApJS, 177, 148
García-Burillo, S., Combes, F., Neri, R., et al. 2007, A&A, 468, L71
Genzel, R., Lutz, D., Sturm, E., et al. 1998, ApJ, 498, 579
Granato, G. L., De Zotti, G., Silva, L., Bressan, A., & Danese, L. 2004, ApJ, 600, 580
Guillard, P., Ogle, P. M., Emonts, B. H. C., et al. 2012, ApJ, 747, 95
Guilloteau, S., & Lucas, R. 2000, in Imaging at Radio through Submillimeter Wavelengths, eds. J. G. Mangum, & S. J. E. Radford, ASP Conf. Ser., 217, 299
Guilloteau, S., Delannoy, J., Downes, D., et al. 1992, A&A, 262, 624
Hardcastle, M. J., Evans, D. A., & Croston, J. H. 2006, MNRAS, 370, 1893
Häring, N., & Rix, H.-W. 2004, ApJ, 604, L89
Higdon, S. J. U., Armus, L., Higdon, J. L., Soifer, B. T., & Spoon, H. W. W. 2006, ApJ, 648, 323
Hill, G. J., Goodrich, R. W., & Depoy, D. L. 1996, ApJ, 462, 163
Ho, L. C., & Keto, E. 2007, ApJ, 658, 314
Holt, J. 2005, Ph.D. Thesis, University of Sheffield
Holt, J., Tadhunter, C. N., & Morganti, R. 2006, Astron. Nachr., 327, 147

Holt, J., Tadhunter, C. N., González Delgado, R. M., et al. 2007, MNRAS, 381, 611

Kaiser, C. R., Schoenmakers, A. P., & Röttgering, H. J. A. 2000, MNRAS, 315, 381

Kaviraj, S., Schawinski, K., Silk, J., & Shabala, S. S. 2011, MNRAS, 415, 3798

Kennicutt, Jr., R. C. 1998, ApJ, 498, 541

Kennicutt, Jr., R. C., Armus, L., Bendo, G., et al. 2003, PASP, 115, 928

Kennicutt, Jr., R. C., Hao, C.-N., Calzetti, D., et al. 2009, ApJ, 703, 1672

Kewley, L. J., Dopita, M. A., Sutherland, R. S., Heisler, C. A., & Trevena, J. 2001, ApJ, 556, 121

King, A. 2003, ApJ, 596, L27

King, A. R., Pringle, J. E., & Hofmann, J. A. 2008, MNRAS, 385, 1621

Krips, M., Crocker, A. F., Bureau, M., Combes, F., & Young, L. M. 2010, MNRAS, 407, 2261

Labiano, A., O'Dea, C. P., Barthel, P. D., de Vries, W. H., & Baum, S. A. 2008, A&A, 477, 491

Lehnert, M. D., Tasse, C., Nesvadba, N. P. H., Best, P. N., & van Driel, W. 2011, A&A, 532, L3

Machalski, J., Kozieł-Wierzbowska, D., Jamrozy, M., & Saikia, D. J. 2008, ApJ, 679, 149

Madrid, J. P., Chiaberge, M., Floyd, D., et al. 2006, ApJS, 164, 307

Magorrian, J., Tremaine, S., Richstone, D., et al. 1998, AJ, 115, 2285

Maiolino, R., Gallerani, S., Neri, R., et al. 2012, MNRAS, 425, L66

Marchesini, D., Celotti, A., & Ferrarese, L. 2004, MNRAS, 351, 733

Marconi, A., & Hunt, L. K. 2003, ApJ, 589, L21

Martel, A. R., Baum, S. A., Sparks, W. B., et al. 1999, ApJS, 122, 81

McCarthy, P. J., Miley, G. K., de Koff, S., et al. 1997, ApJS, 112, 415

McLure, R. J., Jarvis, M. J., Targett, T. A., Dunlop, J. S., & Best, P. N. 2006, MNRAS, 368, 1395

McNamara, B. R., & Nulsen, P. E. J. 2007, ARA&A, 45, 117

McNamara, B. R., & Nulsen, P. E. J. 2012, New J. Phys., 14, 055023

Menci, N., Fiore, F., Puccetti, S., & Cavaliere, A. 2008, ApJ, 686, 219

Merloni, A., & Heinz, S. 2008, MNRAS, 388, 1011

Mezcua, M., Lobanov, A. P., Chavushyan, V. H., & León-Tavares, J. 2011, A&A, 527, A38

Micelotta, E. R., Jones, A. P., & Tielens, A. G. G. M. 2010a, A&A, 510, A37

Micelotta, E. R., Jones, A. P., & Tielens, A. G. G. M. 2010b, A&A, 510, A36

Morganti, R., Oosterloo, T. A., Emonts, B. H. C., van der Hulst, J. M., & Tadhunter, C. N. 2003a, ApJ, 593, L69

Morganti, R., Tadhunter, C. N., Oosterloo, T. A., et al. 2003b, PASA, 20, 129

Morganti, R., Tadhunter, C. N., & Oosterloo, T. A. 2005, A&A, 444, L9

Müller Sánchez, F., Davies, R. I., Eisenhauer, F., et al. 2006, A&A, 454, 481

Murray, N., Quataert, E., & Thompson, T. A. 2005, ApJ, 618, 569

Narayanan, D., Cox, T. J., Kelly, B., et al. 2008, ApJS, 176, 331

Nesvadba, N. P. H., Lehnert, M. D., Eisenhauer, F., et al. 2006, ApJ, 650, 693

Nesvadba, N. P. H., Lehnert, M. D., De Breuck, C., Gilbert, A. M., & van Breugel, W. 2008, A&A, 491, 407

Nesvadba, N. P. H., Boulanger, F., Salomé, P., et al. 2010, A&A, 521, A65

Nesvadba, N. P. H., Boulanger, F., Lehnert, M. D., Guillard, P., & Salome, P. 2011, A&A, 536, L5

O'Dea, C. P. 1998, PASP, 110, 493

O'Dea, C. P., Koekemoer, A. M., Baum, S. A., et al. 2001, AJ, 121, 1915

O'Dowd, M. J., Schiminovich, D., Johnson, B. D., et al. 2009, ApJ, 705, 885

Ogle, P., Antonucci, R., Appleton, P. N., & Whysong, D. 2007, ApJ, 668, 699

Ogle, P., Boulanger, F., Guillard, P., et al. 2010, ApJ, 724, 1193

Pereira-Santaella, M., Diamond-Stanic, A. M., Alonso-Herrero, A., & Rieke, G. H. 2010, ApJ, 725, 2270

Roussel, H., Helou, G., Hollenbach, D. J., et al. 2007, ApJ, 669, 959

Rupke, D. S., Veilleux, S., & Sanders, D. B. 2005, ApJ, 632, 751

Sandage, A. 1967, ApJ, 150, L145

Sandage, A. 1972, ApJ, 178, 25

Saripalli, L., & Mack, K.-H. 2007, MNRAS, 376, 1385

Schawinski, K., Khochfar, S., Kaviraj, S., et al. 2006, Nature, 442, 888

Schawinski, K., Thomas, D., Sarzi, M., et al. 2007, MNRAS, 382, 1415

Schilizzi, R. T., Tian, W. W., Conway, J. E., et al. 2001, A&A, 368, 398

Schmidt, M. 1959, ApJ, 129, 243

Schoenmakers, A. P., de Bruyn, A. G., Röttgering, H. J. A., van der Laan, H., & Kaiser, C. R. 2000, MNRAS, 315, 371

Seymour, N., Symeonidis, M., Page, M. J., et al. 2011, MNRAS, 413, 1777

Siebenmorgen, R., Krügel, E., & Spoon, H. W. W. 2004, A&A, 414, 123

Silk, J., & Nusser, A. 2010, ApJ, 725, 556

Smith, E. P., & Heckman, T. M. 1989, ApJS, 69, 365

Smolčić, V. 2009, ApJ, 699, L43

Smolčić, V., & Riechers, D. A. 2011, ApJ, 730, 64

Sodroski, T. J., Bennett, C., Boggess, N., et al. 1994, ApJ, 428, 638

Solomon, P. M., Rivolo, A. R., Barrett, J., & Yahil, A. 1987, ApJ, 319, 730

Solomon, P. M., Downes, D., Radford, S. J. E., & Barrett, J. W. 1997, ApJ, 478, 144

Spergel, D. N., Verde, L., Peiris, H. V., et al. 2003, ApJS, 148, 175

Strom, R. G., & Willis, A. G. 1980, A&A, 85, 36

Struve, C., & Conway, J. E. 2012, A&A, 546, A22

Sturm, E., González-Alfonso, E., Veilleux, S., et al. 2011, ApJ, 733, L16

Tadhunter, C., Dicken, D., Holt, J., et al. 2007, ApJ, 661, L13

Tadhunter, C., Holt, J., González Delgado, R., et al. 2011, MNRAS, 412, 960

Taylor, M. B. 2005, in Astronomical Data Analysis Software and Systems XIV, eds. P. Shopbell, M. Britton, & R. Ebert, ASP Conf. Ser., 347, 29

Taylor, G. B., Hough, D. H., & Venturi, T. 2001, ApJ, 559, 703

Thomas, D., Maraston, C., Bender, R., & Mendes de Oliveira, C. 2005, ApJ, 621, 673

Tremaine, S., Gebhardt, K., Bender, R., et al. 2002, ApJ, 574, 740

Tremblay, G. R., Chiaberge, M., Donzelli, C. J., et al. 2007, ApJ, 666, 109

Tremblay, G. R., O'Dea, C. P., Baum, S. A., et al. 2010, ApJ, 715, 172

van Gorkom, J. H., Knapp, G. R., Ekers, R. D., et al. 1989, AJ, 97, 708

Veilleux, S., & Osterbrock, D. E. 1987, ApJS, 63, 295

Villar-Martín, M., Humphrey, A., Delgado, R. G., Colina, L., & Arribas, S. 2011, MNRAS, 418, 2032

Voit, G. M. 1992, MNRAS, 258, 841

Willett, K. W., Stocke, J. T., Darling, J., & Perlman, E. S. 2010, ApJ, 713, 1393

Willis, A. G., Strom, R. G., & Wilson, A. S. 1974, Nature, 250, 625

Wright, E. L. 2006, PASP, 118, 1711

York, D. G., Adelman, J., Anderson, Jr., J. E., et al. 2000, AJ, 120, 1579